



The p-n heterojunction with multi-parallel built-in electric fields forms localized "electron sink" for directional non-uniform transfer of photogenerated carriers

Jiliang Niu^{a,b}, Jialiang Lin^b, Jianhua Cheng^{a,b,*}, Yongyou Hu^{a,b}

^a Ministry of Education Key Laboratory of Pollution Control and Ecological Remediation for Industrial Agglomeration Area, College of Environment and Energy, South China University of Technology, Guangzhou 510006, China

^b Guangdong Provincial Key Laboratory of Solid Wastes Pollution Control and Recycling, College of Environment and Energy, South China University of Technology, Guangzhou 510006, China

ARTICLE INFO

Keywords:

Cobalt foam
Electron "pump"
Multi-parallel built-in electric fields
"Electron sinks"
Interfacial enhancement mechanism

ABSTRACT

The internal electric field can induce photogenerated carrier migration. Nevertheless, the spatial arrangement of internal electric fields (independent, series, and parallel) is intricate, which poses a challenge in determining the charge dynamics and process mechanisms. Here, we propose a strategy for in-situ growth of Co_{1-x}S nanosheets and Co_3O_4 nanowires on the surface of cobalt foam (CoF). Each nanosheet is tightly connected to multiple nanowires to form multiple parallel circuits. Notably, DFT and in-situ characterization demonstrate that Co_{1-x}S , with its low Fermi level, can act as an electron "pump" to spontaneously transfer interface electrons to multiple contacting nanowires, forming a multi-parallel built-in electric field (MPBIEF) and generating localized "electron sink". Remarkably, this unique structure promotes the directional asymmetric dispersion movement of carriers under illumination conditions, effectively reducing the recombination probability. Moreover, TDOS electronic state analysis reveals the interface enhancement mechanism of CoF@CS@CO , and a fixed-bed photocatalytic flow treatment system is developed.

1. Introduction

With the advancement of time and technology, more and more new pollutants are being discharged into the water environment. Specifically, the removal of pollutants with low concentrations but high toxicity from industrial and urban wastewater has become a significant challenge [1,2]. Quinolone antibiotics, such as enrofloxacin, levofloxacin and ciprofloxacin, are characterized by a wide antibacterial spectrum, strong antibacterial activity, no cross-resistance with other antibacterial drugs and minimal side effects. Consequently, they are widely used in animal husbandry and aquaculture [3]. Moreover, in livestock farming, chromium (Cr) is usually added to animal feed as a growth regulator. Various types of Cr are added to broiler feeds such as yeast Cr, amino acid Cr integrators, casserole complexes and nicotinate Cr complexes [4]. These micronutrient Cr compounds synergize and enhance insulin activity primarily through Glucose Tolerance Factor (GTF). It is worth noting that Cr(VI) is more toxic than Cr(III) and can

accumulate in living organisms, causing severe illnesses and even death in humans. Unfortunately, most of the additives used in farming are released into the environment through the metabolic system of livestock. Additionally, antibiotics can complex with hexavalent chromium to form complex contaminants that are difficult to remove [5]. Consequently, the countermeasure has become a key step in the current water pollution control, i.e., the adoption of efficient wastewater treatment technologies that can treat Cr(VI) and quinolone antibiotics [6].

Semiconductor photocatalysts can directly transfer and utilize solar energy to generate photogenerated carriers and derive a series of active species, which, together with photogenerated electrons, are quickly involved in the degradation of antibiotics, and can reduce Cr(VI) to Cr(III), thus realizing the simultaneous removal of complex pollutants [7]. However, the practical application of conventional photocatalysts is severely limited due to three main issues: 1) the difficulty of recycling powdered catalysts and the poor stability of loaded catalysts developed on inert substrates; 2) concerns about the direction of transfer and

* Corresponding author at: Ministry of Education Key Laboratory of Pollution Control and Ecological Remediation for Industrial Agglomeration Area, College of Environment and Energy, South China University of Technology, Guangzhou 510006, China.

E-mail address: jhcheng@scut.edu.cn (J. Cheng).

<https://doi.org/10.1016/j.apcatb.2024.123825>

Received 17 November 2023; Received in revised form 22 January 2024; Accepted 5 February 2024

Available online 7 February 2024

0926-3373/© 2024 Elsevier B.V. All rights reserved.

dispersion of photogenerated e^- and h^+ on the catalyst surface to reduce the compounding efficiencies; and 3) the practical need for a complete system solution that is safe to use, simple to operate and inexpensive to implement rather than focusing solely on the catalyst itself [8]. Although various modification strategies including morphological modification, elemental doping and construction of heterojunction have been proposed to improve the photocatalytic efficiency, the kinetics of separation, migration and output of photoexcited charge carriers, which fundamentally determines the photocatalytic activity, are still sluggish and disordered [9,10].

Internal electric field at the interface of a heterojunction photocatalyst serves as an intrinsic driving force that regulates the transport of photogenerated carriers upon excitation and determines their dynamics and behavior [11,12]. It has gained increasing prominence and recently acquired significant attention in the field of photocatalysis. While most studies on the internal electric field have provided only qualitative evidence for its existence, such as demonstrating that it enhances the photocatalytic performance of g-C₃N₄ plane [13], there is limited understanding of its various forms of distribution from the interface to the molecular scale (including independent, series and parallel forms), as well as of how its geometry and arrangement affects carrier transport and action. Given the limitations of existing research methods, an innovative and general strategy for synthesizing heterojunctions with specific configuration is urgently needed. By studying the distribution of electron-hole pairs accumulated at the heterojunction interface and the photocatalytic carrier separation, we look forward to explore the mechanism behind the photocatalytic activity of the electric field inside the aligned configuration [14]. Furthermore, there is scarce literature on in-situ growth of active components on recyclable substrates or construction of photocatalytic flow-through processing devices [15].

Co_{1-x}S nanosheets and Co₃O₄ nanowires are metallically bonded by in-situ growth on the CoF surface. Due to the contact between multiple Co_{1-x}S nanosheets and Co₃O₄ nanowires, multiple parallel circuits are established at the interface of Co_{1-x}S. Experimental and computational simulations demonstrate that because of the low Fermi level of the Co_{1-x}S plane surface, it can act as an electron "pump" to spontaneously transport electrons to the interface of Co₃O₄ nanowires, thus forming multi-parallel built-in electric fields (MPBIEF) on the 2D nanosheets of Co_{1-x}S. This presence disrupts the symmetry of charge distribution on the plane of Co_{1-x}S, creating localized "electron sink" (representing electron pooling regions). MPBIEF dominates the directional transfer motion of the carriers, resulting in a non-uniform dispersion of charges in the Co_{1-x}S plane and reducing the recombination probability. This ingenious configuration forms a p-n heterostructure that enhances the photocatalytic performance for simultaneous degradation of enrofloxacin (ENR) and reduction of Cr(VI) in CoF@CS@CO. Furthermore, considering the complexity of water pollution, we also investigated how pH value, organic species and inorganic salts affect the photocatalytic activity. This study systematically elucidates the effect of MPBIEF on photogenerated carriers and provides a feasible approach for designing heterojunctions with different configurations of built-in electric fields.

2. Experimental section

2.1. Synthesis of CoF@Co_{1-x}S, CoF@Co₃O₄, and CoF@CS@CO

The production process of CoF@Co_{1-x}S@Co₃O₄ (abbreviated as CoF@CS@CO) consists of several steps. First, a 2 cm × 2 cm cobalt foam (CoF) was treated with hydrochloric acid solution in an ultrasonic bath for 5 min to remove the oxide layer. Subsequently, several ultrasonic cleanings were performed with acetone, deionized water and ethanol. That treated CoF was then placed into an alumina crucible with sulfur powder at the bottom to facilitate the growth of Co_{1-x}S on its surface. Typically, vulcanization is carried out at 250 °C for 2 h under an inert Ar atmosphere, followed by annealing at 400 °C for 3 h. After cooling, the desired CoF@Co_{1-x}S was obtained. To synthesize CoF@CS@CO, the

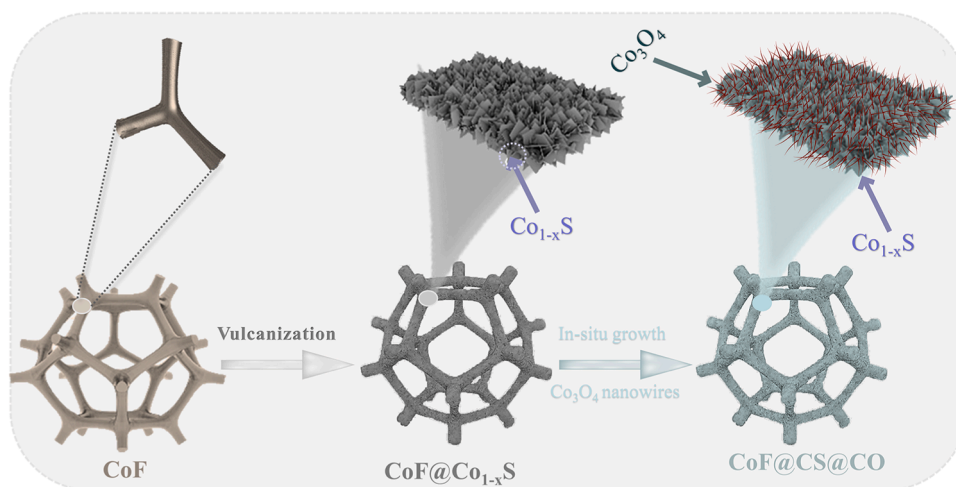
resulting CoF@Co_{1-x}S, along with 19 mmol Co(NO₃)₂·6 H₂O, 25.0 mmol urea and 10.0 mmol NH₄F were simultaneously added into a stainless steel autoclave lined with Teflon containing 60 mL deionized water. The mixture was then heated at 120 °C for 10 h. At the end of the reaction, the cobalt foam was washed, dried, and calcined under nitrogen atmosphere at 300 °C for 2 h. This allowed the growth of Co₃O₄ nanowires on the surface of the CoF, forming the CoF@CS@CO. Using the same method, CoF@Co₃O₄ was obtained by growing Co₃O₄ nanowires on the CoF surface without Co_{1-x}S. The schematic representation of the production process for CoF@CS@CO has been shown in Scheme 1.

2.2. Photocatalytic activity measurements

Photocatalytic performance of the prepared photocatalyst was evaluated by degrading ENR and reducing Cr(VI) under visible light irradiation using a 300 W xenon lamp with a 420 nm cut-off filter. 50 mL aqueous solution containing contaminants (ENR and Cr(VI) at a concentration of 10 mg/L, respectively) and photocatalyst (10 mg) was stirred in the dark for 30 min to fully adsorb the pollutants. Subsequently, the above solution was subjected to photocatalytic reaction under a light source. Aliquot of 1.0 mL was collected at regular intervals for further analysis. The concentration of ENR was determined by ultra-high liquid chromatography (HPLC) with a detection wavelength of 272 nm. Mobile phase was 0.1% solution of formic acid and acetonitrile at a flow rate of 1 mL·min⁻¹ in the ratio of 70:30. For each analysis, 10 μL of the sample was injected. The concentration of Cr(VI) was determined at 540 nm using a UV-2700 UV-Vis spectrophotometer. To ensure reproducibility, three tests were performed for each condition to produce an average result. By varying the experimental parameters, the effects of pH, organic matter, inorganic salts and other experimental factors were investigated. Moreover, the photocatalytic stability was evaluated by cycling experiments. A liquid chromatography-mass spectrometry (LC-MS) system was used to detect the intermediates of ENR degradation.

2.3. Fixed-bed photocatalytic system

A fixed-bed photocatalytic system used in this study aimed to achieve flow treatment of composite polluted wastewater by utilizing the highly porous structure of CoF@CS@CO. The unique structure of CoF@CS@CO solved two challenges. Firstly, it eliminates the problem of secondary pollution caused by the dense accumulation of powdered catalysts, which impedes the flow and leads to fluid loss. Secondly, it overcomes the problem of limited fluid and light penetration caused by the dense structure of thin film materials. To construct the system, a transparent polycarbonate cylinder reactor with dimensions of φ6.4 cm × 13.5 cm was used. Two pieces of CoF@CS@CO with a thickness of 1.0 cm were cut to an appropriate size and loaded into the reactor. To ensure effective light transmission, the spacing between catalysts was greater than 5.0 cm so as to prevent light from being blocked. During the experiments, a peristaltic pump was employed to provide a constant flow rate of 5 mL/min and a hydraulic retention time (HRT) of 87 min under xenon lamp irradiation. In experiments using real sunlight, the flow rate was adjusted to 2.5 mL/min and the HRT was extended to 114 min. Water sample (1.0 mL) was collected from the collection area every 100 min to monitor the residual concentrations of ENR and Cr(VI) as an indicator of treatment efficacy. For light sources, a 300 W xenon lamp with a filter (≥ 420 nm) or real sunlight was used. Sunlight was selected from a sunny day in Guangzhou, China (23°8' N, 113°17' E) in 2023 from 9:00 am to 17:00 PM. In order to measure the remaining total organic carbon (TOC) in the wastewater, an Apollo 9000 TOC analyzer (Teck Madorman, Atlanta, USA) was employed.



Scheme 1. Schematic illustration for synthetic procedure of CoF@CS@CO.

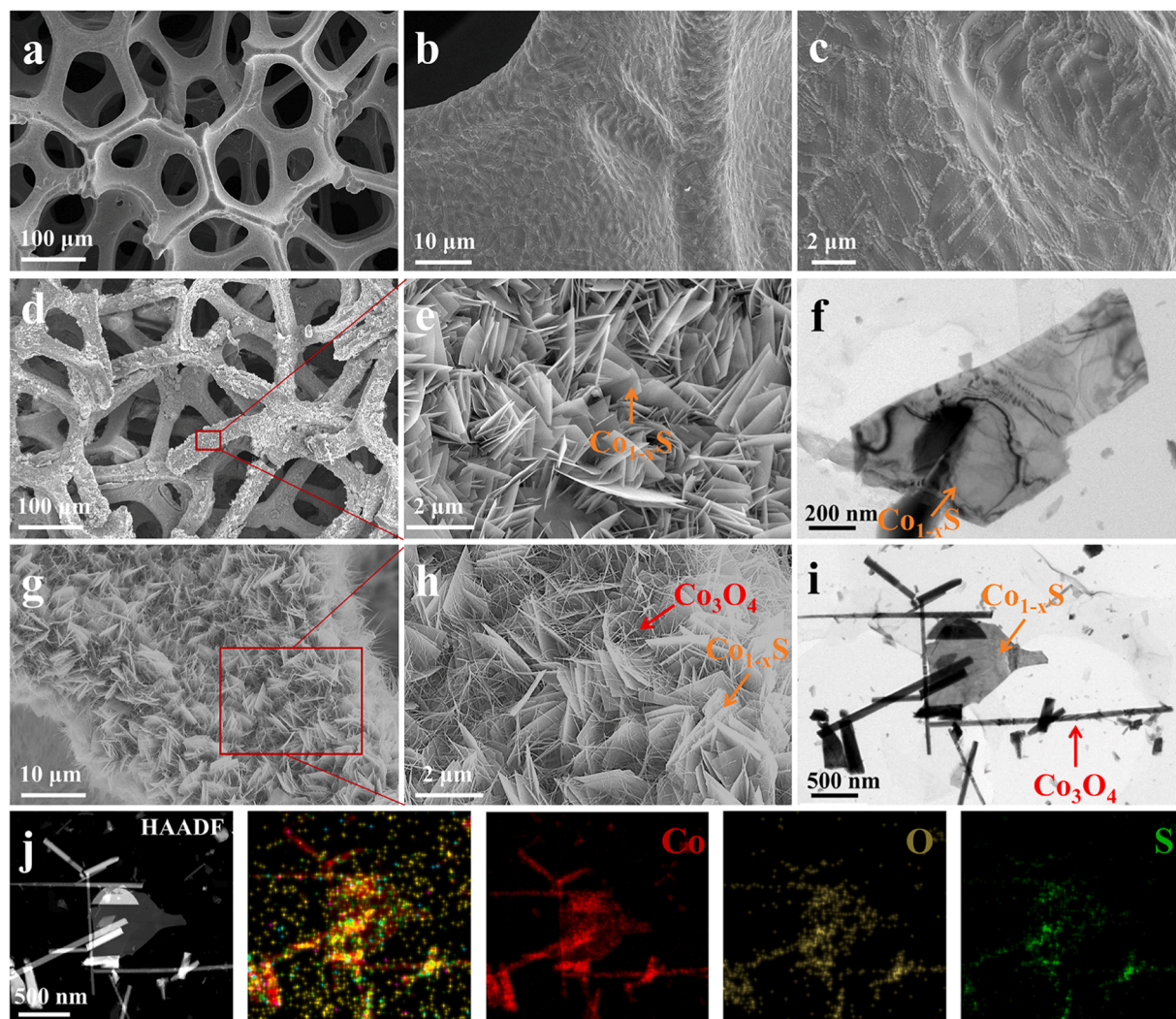


Fig. 1. SEM images of the original CoF at low magnification (a) and high magnification (b-c); SEM images of CoF@Co_{1-x}S at low magnification (d) and high magnification (e) and the corresponding TEM images (f); SEM images of CoF@CS@CO at low magnification (g) and high magnification (h) and the corresponding TEM images (i); STEM image and the corresponding EDX spectral contours (j) of CoF@CS@CO.

3. Results and discussion

3.1. Structural and morphological analyses

Scanning electron microscopy (SEM) and transmission electron microscopy (TEM) were used to characterize the morphology of the catalyst. As shown in Fig. 1a, the pristine CoF exhibits an interconnected 3D structure with ultra-high porosity, which is critical for the actual fluidized treatment of wastewater. Fig. 1b-c are magnified images of bare CoF, showing a smooth surface with ample active sites provided by subsequent in-situ growth of the active species. After Co_{1-x}S is grown in-situ on the surface of CoF, its surface becomes rough and is completely covered (Fig. 1d). Moreover, the magnified SEM image is shown in Fig. 1e. It is found that Co_{1-x}S is a uniformly shaped nanosheet with high density, which grows vertically in-situ on the CoF surface and is well separated from each other. The corresponding TEM image (Fig. 1f) shows that Co_{1-x}S is a rectangular-like 2D nanosheet structure. The high-resolution transmission electron microscopy (HRTEM) images of Co_{1-x}S in Figs. S1a-b show that the lattice fringe spacing is about 0.19 nm, corresponding to the (102) plane of the hexagonal Co_{1-x}S . Furthermore, as shown in Figs. S1c-f, the EDS mapping results of $\text{CoF@Co}_{1-x}\text{S}$ show a uniform distribution of Co and S elements, which further confirms the in-situ growth of Co_{1-x}S on its surface. The intercalated nanosheet cluster structure composed of these vertical nanosheets can make the incident light reflect several times inside them, reduce the direct reflection and improve the utilization rate of light. Moreover, the nanosheet structure has a large specific surface area, which can provide an extraordinary number of reaction sites [16]. As shown in Fig. 1g, after the second step of in-situ growth, a large number of Co_3O_4 nanowires appear around the Co_{1-x}S nanosheets. The enlarged image shows that Co_3O_4 nanowires are densely wrapped around Co_{1-x}S nanosheets, and each Co_{1-x}S nanosheet will be in close contact with multiple Co_3O_4 nanowires. This structure consisting of Co_{1-x}S nanosheets and multiple Co_3O_4 nanowires can form a p-n heterojunction with MPBIEF to achieve localized "electron sink", which can promote the

directional movement of charge under visible light irradiation and achieve the inhomogeneous dispersion of Co_{1-x}S plane charges, suppressing the contact probability of photogenerated e^- and h^+ [17]. TEM and EDX were used to further demonstrate the successful construction of this unique structure. The TEM image of Fig. 1i clearly shows that the Co_{1-x}S nanosheet will be in close contact with multiple Co_3O_4 nanowires. Notably, the structure is incomplete because the samples are obtained by slight scraping directly on the CoF@CS@CO surface. HRTEM further examined the heterogeneous interface structure between Co_{1-x}S and Co_3O_4 , with blue labeled regions for Co_{1-x}S and yellow labeled regions for Co_3O_4 . The lattice stripes at 0.19 nm and 0.24 nm in the blue and yellow labeled regions coincide with the (102) and (311) planes of Co_{1-x}S and Co_3O_4 , respectively, verifying the successful construction of the $\text{Co}_{1-x}\text{S}/\text{Co}_3\text{O}_4$ heterojunction (Figs. S2a-c). Fig. 1j shows the results of TEM energy dispersive X-ray spectroscopy (EDX) mapping images, where Co elements are distributed throughout the selected region, while O and S elements only in the nanowire and nanosheet regions, respectively, suggesting that Co_{1-x}S nanosheets and Co_3O_4 nanowires grow uniformly on the CoF surface. Fig. S3a shows the SEM image of $\text{CoF@Co}_3\text{O}_4$, which reveals that the surface of CoF is completely covered by Co_3O_4 nanowires after in-situ growth. In addition, Figs. S3b-c display the approximately 60 nm diameter and smooth surface of the Co_3O_4 nanowires. Fig. S3e depicts an enlarged HRTEM image of Co_3O_4 , from which a set of lattice fringes with a width of 0.24 nm can be observed associated with the (311) face of cubic Co_3O_4 . Additionally, the EDS results in Figs. S3f-h show a uniform distribution of Co and O elements.

The crystal structures of all samples were analyzed by X-ray diffraction (XRD). As shown in Fig. 2a, the pristine CoF shows three characteristic peaks at $2\theta = 44.2^\circ$, 51.5° and 75.8° , corresponding to the Co^0 (111), (200) and (220) planes (PDF#15-0806), respectively, indicating that CoF is composed of metallic cobalt. For $\text{CoF@Co}_3\text{O}_4$, $\text{CoF@Co}_{1-x}\text{S}$ and CoF@CS@CO composites, new diffraction peaks appear in addition to Co^0 . New diffraction peaks for $\text{CoF@Co}_3\text{O}_4$ appear at $2\theta = 31.1^\circ$, 36.8° , 59.3° and 65.2° , corresponding to the Co_3O_4 (220),

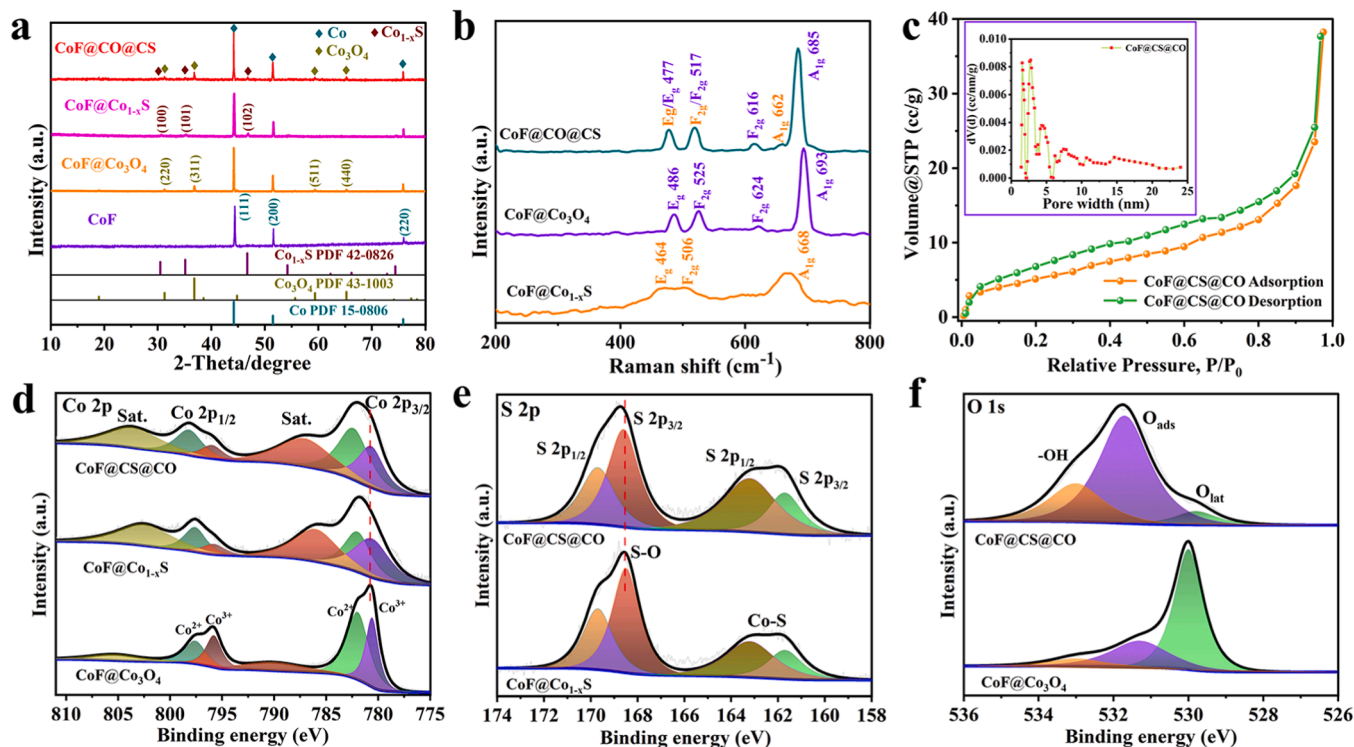


Fig. 2. XRD (a) and Raman spectroscopy (b) of different samples; N_2 adsorption and desorption of CoF@CS@CO and isothermal pore size dispersion (c); High-resolution spectra of Co 2p, S 2p, and O 1s (d-f) of different samples.

(311), (511) and (440) planes (PDF#43-1003), respectively. The results showed that Co_3O_4 nanowires were successfully grown in-situ on the CoF surface. New characteristic peaks were detected at $2\theta = 30.5^\circ$, 35.2° and 46.8° for the sulfurized and annealed $\text{CoF@Co}_{1-x}\text{S}$, corresponding to the Co_{1-x}S (100), (101), and (102) planes (PDF#42-0826), respectively. As expected, the new diffraction pattern of the CoF@CS@CO heterojunction shows a mixture of Co_3O_4 and Co_{1-x}S crystalline phases, indicating that this marks the in-situ growth of both semiconductors on CoF surface [18]. Meanwhile, Raman spectra were recorded to determine the structural characteristics of the sample, as exhibited in Fig. 2b. Peaks of $\text{CoF@Co}_{1-x}\text{S}$ around 464, 506 and 668 cm^{-1} are corresponding to Co_{1-x}S as well as the E_g , F_2g and A_1g modes of the crystal, respectively [19]. The peaks appearing at 486, 525, 624 and 693 cm^{-1} for $\text{CoF@Co}_3\text{O}_4$ should be attributed to the E_g , F_2g , F_2g , and A_1g modes of Co_3O_4 [20]. CoF@CS@CO showed bands corresponding to all functional groups of Co_{1-x}S and Co_3O_4 , with peaks appearing redshifted or blue-shifted, suggesting strong interactions and electron transfer between Co_{1-x}S and Co_3O_4 metal sites [21]. FT-IR absorption spectra (Fig. S4) showed distinct peaks at 643 and 552 cm^{-1} , confirming the presence of Co_3O_4 nanowires in $\text{CoF@Co}_3\text{O}_4$ [22]. The IR spectral analysis revealed strong peaks at 679 and 456 cm^{-1} , which are attributed to the stretching vibrations of S-S and Co-S bonds, confirming the presence of Co_{1-x}S nanosheets on the CoF surface in $\text{CoF@Co}_{1-x}\text{S}$ [23]. Notably, the IR spectrum of CoF@CS@CO was a mixture of $\text{CoF@Co}_3\text{O}_4$ and $\text{CoF@Co}_{1-x}\text{S}$, with changes in peak positions, indicating a strong interaction between Co_{1-x}S and Co_3O_4 . The nitrogen adsorption-desorption isotherm and pore size distribution of CoF@CS@CO displayed an IV-type isotherm, with steep absorption at low pressures, demonstrating the presence of typical micropores. In addition, hysteresis loops were also observed at high pressures, which indicated the occurrence of mesoporous pores (Fig. 2c). The specific surface area of CoF@CS@CO was $108.4\text{ m}^2\text{g}^{-1}$, with a pore size distribution mainly between 1–5 nm. Noteworthy, the large surface area and micro-mesoporous structure facilitated the exposure of active sites and rapid mass transfer during the photocatalytic process, enhancing the catalytic efficiency for the synergistic removal of ENR and Cr(VI) [24].

The surface valence and local micro-environment of the photocatalyst were determined by using X-ray photoelectron spectroscopy (XPS). Furthermore, the interactions amongst the various components in CoF@CS@CO were identified. The measured spectra of $\text{CoF@Co}_3\text{O}_4$, $\text{CoF@Co}_{1-x}\text{S}$ and CoF@CS@CO have been shown in Fig. S5. Co, O and S are all visible elements in CoF@CS@CO , which further demonstrates the formation of MPBIEF with p-n heterojunction $\text{Co}_{1-x}\text{S}/\text{Co}_3\text{O}_4$. The produced C element is due to the absorption of CO_2 from the air. The XPS spectra of Co 2p for $\text{CoF@Co}_3\text{O}_4$ and $\text{CoF@Co}_{1-x}\text{S}$ shown in Fig. 2d contain two spin orbital doublet states. The first set of peaks can be decomposed into two peaks with binding energies of 794.9 and 796.7 eV, which should be ascribed to Co^{3+} and Co^{2+} of Co $2p_{3/2}$, respectively. The other set of peaks can be similarly decomposed into 779.4 and 781.1 eV, corresponding to Co^{3+} and Co^{2+} of Co $2p_{1/2}$, respectively [25]. The results show that the Co2p binding energy of CoF@CS@CO is positively shifted compared with that of $\text{CoF@Co}_3\text{O}_4$ and $\text{CoF@Co}_{1-x}\text{S}$, which suggests the existence of electronic coupling and electron transfer between Co_{1-x}S and Co_3O_4 [26]. The high-resolution S 2p spectra of $\text{CoF@Co}_{1-x}\text{S}$ and CoF@CS@CO show two characteristic peaks at 161.7 and 163.2 eV, which are derived from the S $2p_{3/2}$ and S $2p_{1/2}$ characteristic peaks of the Co-S bond, respectively. The presence of S-O bonds can also be clearly observed in Fig. 2e, which may be due to the adsorption of oxygen from air [27]. We also obtained O 1s high-resolution spectra of $\text{CoF@Co}_3\text{O}_4$ and CoF@CS@CO samples (Fig. 2f). In general, the O 1s XPS spectrum is deconvoluted into three regions: (i) surface lattice oxygen (Olat), (ii) surface adsorbed oxygen (Oads) and (iii) surface hydroxyl (-OH) [28]. Lattice oxygen reveals the interaction between metal and oxygen, while surface-adsorbed oxygen facilitates photocatalytic reactions and promotes the formation of oxygen-containing active species. The efficiency

of photocatalytic degradation can be improved by increasing the adsorption rate of CoF@CS@CO [29].

3.2. Photocatalytic removal studies

Fig. S6 shows the adsorption curves of CoF, $\text{CoF@Co}_3\text{O}_4$, $\text{CoF@Co}_{1-x}\text{S}$ and CoF@CS@CO on ENR and Cr(VI) over time. Under dark conditions, CoF hardly shows any adsorption characteristics, while the other three substances show similar adsorption behaviors. The adsorption rate of CoF@CS@CO decreased significantly after 30 min of adsorption on ENR, and the adsorption equilibrium was reached after 45 min. In the adsorption of Cr(VI), the adsorption rate also decreased significantly after 30 min of adsorption. In order to shorten the reaction time and improve the reaction efficiency, 30 min was selected as the dark reaction time [30]. The development of photocatalytic systems capable of simultaneous degradation of antibiotics and reduction of Cr(VI) is particularly revealing when compared to systems for removal of individual pollutants, which have far-reaching implications in practice. Moreover, the performance of different catalysts for the simultaneous removal of ENR and Cr(VI) composite pollutants was tested under visible light irradiation. As shown in Fig. 3a, the degradation rate of ENR by CoF@CS@CO reached 96.9% and the reduction rate of Cr(VI) attained 98.5% after 90 min of visible light irradiation. The first-order kinetic constants (k) for the degradation of ENR and reduction of Cr(VI) by CoF@CS@CO were also proved to have the highest k values of 0.0366 and 0.0455 min^{-1} , respectively. Where the k values of CoF@CS@CO for the degradation of ENR were 3.45 and 2.58 times higher than those of $\text{CoF@Co}_{1-x}\text{S}$ and $\text{CoF@Co}_3\text{O}_4$, and the k values for the reduction of Cr(VI) were 5.23 and 3.12 times higher than those of $\text{CoF@Co}_{1-x}\text{S}$ and $\text{CoF@Co}_3\text{O}_4$, respectively, as exhibited in Fig. S7. In addition, the removal rates were almost zero when visible light irradiated the ENR and Cr(VI) composite pollutant solution without catalyst, indicating that the pollutants could be stabilized in the natural environment (Fig. S8). In the single pollutant system, the photodegradation efficiency of ENR is only 55.6%, while the photoreduction efficiency of Cr(VI) is only 59.7%. However, in the system where ENR and Cr(VI) coexisted, there is a significant improvement in the removal efficiency of ENR and Cr(VI). The improved photocatalytic performance of CoF@CS@CO in ENR and Cr(VI) co-existing systems can be attributed to the synergistic effect between photocatalytic reduction and oxidation processes. Under coexisting conditions, ENR acts as a photogenerated hole scavenger being oxidized, while Cr(VI) serves as a photogenerated electron acceptor similarly reduced [31].

3.3. Condition-affected experiment of CoF@CS@CO

Initial pH value of the substrate is one of the key factors affecting the photocatalytic performance and should be included in the study. Among them, ENR molecules can be categorized into protonation (H_2Q^+ , $\text{pH} < 6.02$), zwitterion (HQ^\pm , $6.02 < \text{pH} < 8.25$) and anion (Q^- , $\text{pH} > 8.25$) based on the initial aqueous pH [32]. The surface charge of CoF@CS@CO in a photocatalytic system the positive at $\text{pH} < 6.45$ and negative at $\text{pH} > 6.45$. Consequently, electrostatic repulsion between the photocatalyst and the protonated or anionic ENR under acidic and alkaline conditions limits the adsorption of active sites and impedes photocatalytic degradation (Fig. S9). Therefore, as shown in Fig. 3b, the highest removal efficiency of ENR by CoF@CS@CO is achieved at pH 7 under the condition of coexistence of ENR and Cr(VI). Under the coexistence of pollutants, the reduction efficiency of Cr(VI) decreases gradually with the increase of solution pH. This may be due to the fact that Cr(VI) is mainly present in the form of $\text{Cr}_2\text{O}_7^{2-}$ under acidic conditions and CrO_4^{2-} under alkaline conditions. Furthermore, CrO_4^{2-} [$\text{E}_0(\text{CrO}_4^{2-}/\text{Cr}(\text{OH})_3) = -0.13\text{ eV vs NHE}$] is more difficult to reduce to Cr(III) than $\text{Cr}_2\text{O}_7^{2-}$ [$\text{E}_0(\text{Cr}_2\text{O}_7^{2-}/\text{Cr}^{3+}) = +1.36\text{ eV vs NHE}$] [33]. As a result, Cr(VI) is easily reduced to Cr(III) under acidic conditions, while it is difficult under alkaline conditions. In addition, Cr(III) generated under alkaline

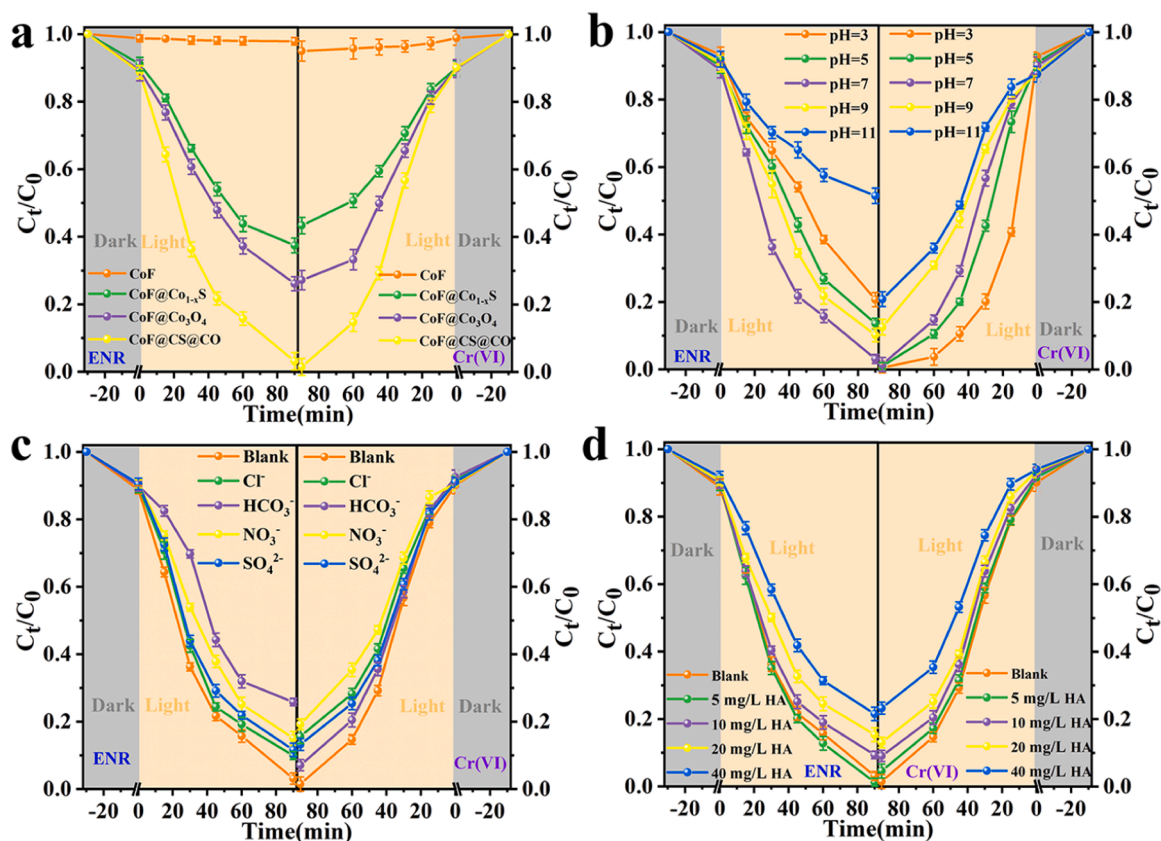


Fig. 3. The catalytic efficiency of different catalysts in dark + light environment under the coexistence of ENR and Cr(VI) (a); Effect of pH (b), inorganic anion (c), and HA (d) on the photocatalytic activity of CoF@CS@CO under the coexistence of ENR and Cr(VI).

conditions will form $\text{Cr}(\text{OH})_3$ to cover the active site on the catalyst surface, thus reducing the degradation of ENR and the reduction of Cr (VI). Considering the catalytic activity and the operability of the experiment, pH 7 is chosen as the initial value in this study. In general, there are some common inorganic ions in the actual wastewater, which may affect the photocatalytic performance. Therefore, the effect of typical inorganic ions on the efficiency of CoF@CS@CO photocatalytic synchronous removal of ENR and Cr(VI) was investigated, as shown in Fig. 3c. Obviously, the presence of Cl^- , NO_3^- and SO_4^{2-} slightly affected the degradation efficiency of ENR. In contrast, ENR degradation can be significantly inhibited in the presence of CO_3^{2-} , which may be attributed to the fact that CO_3^{2-} depletes some of the active species and produces weaker free radicals, leading to a decrease in the efficiency of ENR degradation [34]. The addition of inorganic anions also slightly affects the reduction of Cr(VI), probably because these ions compete with Cr (VI) for the photocatalytic active sites and hinder the reaction. Additionally, the effect of dissolved organic matter (humic acid) on the photocatalytic process has been investigated, since humic acid (HA) is commonly found in water as a macromolecular organic matter. As shown in Fig. 3d, the degradation efficiency of ENR increases when the concentration of HA is varied from 0 to 5 mg/L. This is mainly due to the fact that HA is a photosensitizer that can directly form $^3\text{HA}^*$ or produce free radicals to act on ENR. However, with further increase in HA concentration, the photoactivity was inhibited due to competition for reaction sites and the light shielding effect. With the increase of HA concentration, the reduction efficiency of Cr(VI) decreased slightly, primarily due to the shading effect of HA [35].

3.4. Reusability and stability of CoF@CS@CO composites

In practical applications, the stability and recyclability of catalysts are key issues. Therefore, the recycling experiments of CoF@CS@CO

photocatalyst were carried out, and the results have been shown in Fig. 4a. Since the active component are directly grown in-situ on the CoF surface, the CoF@CS@CO can be conveniently retrieved from the waste liquid with tweezers after reaction, and it is suggested to utilize similar magnetic recovery (cobalt metal has strong magnetic properties). After recovery, the composite was washed with deionized water and proceeded to the next cycle directly. The efficiency of photocatalytic degradation of ENR and reduction of Cr(VI) remained above 80% after 10 cycles, which demonstrated that the CoF@CS@CO composite has the potential to be a convenient and reusable photocatalyst. In order to further investigate the reason for the excellent cycling performance of the catalysts, different elements on the catalyst were detected by XPS. The chemical composition and electronic states of the CoF@CS@CO surface were investigated by XPS. As shown in Fig. S10a, the survey spectrum shows the emergence of a new peak of Cr 2p. No chemical shifts of Co 2p, S 2p and O 1s were observed by XPS fitting analysis, indicating that the catalyst was chemically stable after the reaction, and the catalyst decay or leaching was not obvious (Figs. S10b-d) [36]. Additionally, the peaks at 576.7 and 586.3 eV can be attributed to the Cr $2p_{3/2}$ and Cr $2p_{1/2}$ orbitals of Cr(III), whereas the peaks at 578.7 and 588.2 eV should be corresponded to the Cr $2p_{3/2}$ and Cr $2p_{1/2}$ orbitals of Cr(VI), suggesting the transformation of Cr(VI) into Cr(III) (Fig. 4b) [37]. C 1s indicates an additional O-C=O bond (288.7 eV) on the catalyst surface after the reaction, which may be a degradation intermediate product adsorbed on the catalyst surface (Fig. 4c) [38]. The leaching concentrations of different elements in each cycle were also determined in this study. As can be seen in Fig. 4d, slight component leaching occurs in almost every cycle, resulting in a slight decrease in the catalytic activity. The single maximum leaching amounts of Co and S did not exceed 0.0542 mg/L and 0.0193 mg/L, respectively. The United States Environmental Protection Agency requires that the concentration of sulfide in tap water does not exceed 1.3 mg/L, and the environmental

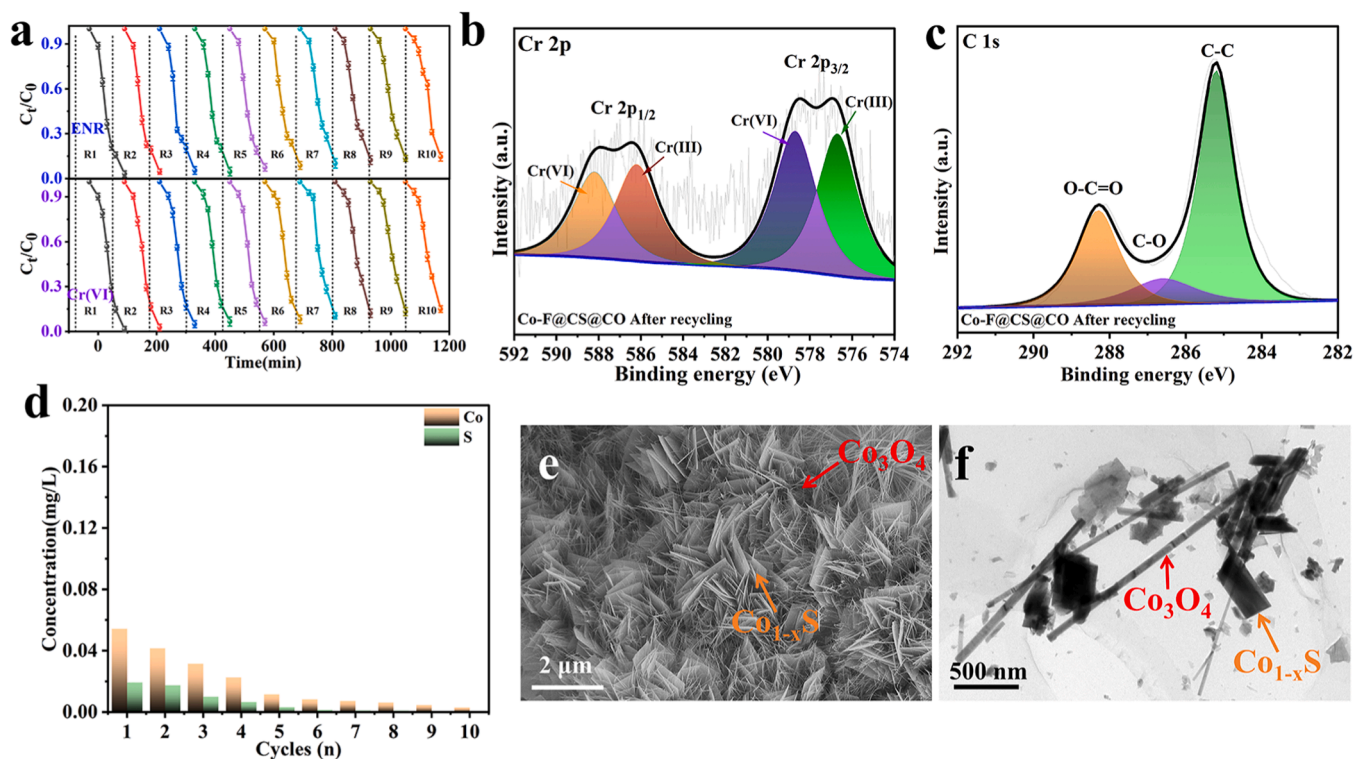


Fig. 4. Cycling test for simultaneous degradation of ENR and reduction of Cr(VI) over CoF@CS@CO catalyst (a); High-resolution spectra of Cr 2p (b) and C 1s (c) after cycling; Residual elemental concentration of the solution after each cycling (d); SEM images (e) and TEM images (f) after cycling of CoF@CS@CO.

standard of United States stipulates a maximum allowable concentration of Co in irrigation water is 0.2 mg/L. The element leaching rate of catalyst during the reaction process is significantly lower than the above standard, which indicates the high stability and safety of the use process [39]. In addition, SEM images and XRD patterns of fresh and recycled CoF@CS@CO photocatalysts were tested to characterize the physical structure and morphology of the photocatalysts before and after the photocatalytic degradation reaction. As shown in Fig. 4e-f, the morphology of CoF@CS@CO does not change much after cycling, and the Co_{1-x}S nanosheets are still in contact with numerous Co_3O_4 nanowires. The XRD patterns show that the CoF@CS@CO phase structure remains intact after repeated use (Fig. S11). This demonstrates that the catalyst possesses good photostability and cycle stability.

3.5. Photocatalytic mechanism

The light absorption properties of CoF@ Co_{1-x}S , CoF@ Co_3O_4 and CoF@CS@CO heterojunctions have been recorded by ultraviolet-visible diffuse reflectance spectroscopy (UV-Vis DRS). As shown in Fig. 5a, the Co^{3+} and Co^{2+} in CoF@ Co_3O_4 are in octahedral and tetrahedral positions, respectively, resulting in broad absorption peaks between 350 nm and 500 nm for Co_3O_4 [40]. However, due to the intercalated structure consisting of nanosheets, Co_{1-x}S has a strong full-spectrum absorption, which can lead to multiple internal scattering/reflection of light [41]. Owing to the unique structure of Co_{1-x}S , the composite CoF@CS@CO samples also show significant absorption in the visible region, indicating that CoF@CS@CO can effectively utilize visible light. In particular, the band gap between the monomer and composite is calculated according to the Kubelka-Munk formula (Eq. 1):

$$\alpha h\nu = A(h\nu - E_g)^{2/n} \quad (1)$$

Where α , h , ν , E_g and A represent the absorption coefficient, Planck's constant, optical frequency, bandgap energy and constant, respectively, while Co_{1-x}S and Co_3O_4 are indirect, so n is equal to 4. Fig. 5b shows the

calculated E_g of 1.84, 1.35, and 1.05 eV for CoF@ Co_3O_4 , CoF@ Co_{1-x}S and CoF@CS@CO catalysts, respectively [42,43]. The smaller bandgap of the composites compared to the pristine CoF@ Co_3O_4 and CoF@ Co_{1-x}S suggests the formation of p-n heterojunctions for Co_3O_4 and Co_{1-x}S .

Mott-Schottky (M-S) tests were used to explore the semiconductor types of CoF, Co_{1-x}S and Co_3O_4 . As shown in Fig. S12, Co_{1-x}S is categorized as an n-type semiconductor with a positive curve slope, while Co_3O_4 is classified as a p-type semiconductor with a negative slope. The CoF test result is a straight line, indicating that it is not a semiconductor material that only acts as a conductive substrate and does not participate in the reaction. As shown in Fig. S13, the M-S diagram of CoF@CS@CO shows an inverted "V-shape", which is attributed to the formation of p-n heterojunction after coupling of n-type Co_{1-x}S with p-type Co_3O_4 , which leads to the Fermi level displacement, i.e., flat band potential shifts. The above results confirmed that Co_{1-x}S and Co_3O_4 formed p-n heterojunction [44]. The flat band potential (E_{fb}) of the sample with respect to the SCE can be obtained by testing. Moreover, the approximate Fermi energy level (E_f) can be acquired from the flat band potential. In general, the conduction band potential (E_{CB}) of n-type semiconductors is more negative than their E_{fb} by about -0.1 V. In contrast, the valence band potential (E_{VB}) of p-type semiconductors is about 0.1 V higher than their E_{fb} . By calculation, the E_{CB} and E_{VB} of Co_{1-x}S and CoF@ Co_3O_4 are -0.37 and 0.80 eV vs. NHE ($E_{NHE} = E_{SCE} + 0.24$), respectively [45]. The E_{VB} for Co_{1-x}S and E_{CB} for Co_3O_4 can be obtained by the energy band formula (Eq. 2):

$$E_{VB} = E_{CB} + E_g \quad (2)$$

Combined with the E_g values of CoF@ Co_{1-x}S and CoF@ Co_3O_4 in the reported work (1.35 V and 1.84 eV), it can be roughly determined that the E_{VB} and E_{CB} of CoF@ Co_{1-x}S and CoF@ Co_3O_4 are 0.96 and -1.04 eV, respectively [46].

In addition to light absorption, the separation efficiency of photo-generated carriers is another important factor in determining the photocatalytic performance. The separation of photogenerated electrons

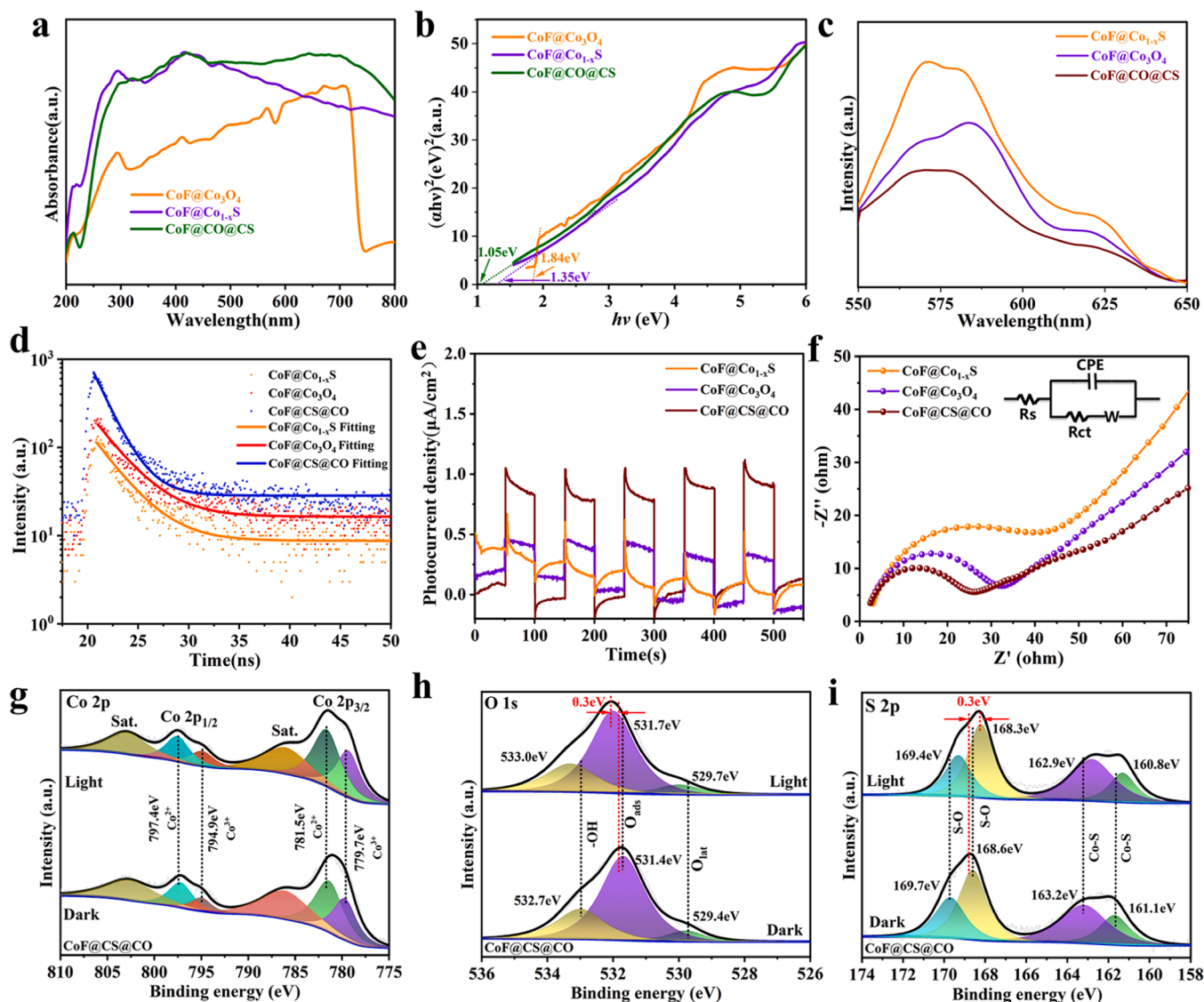


Fig. 5. UV-vis DRS (a) and corresponding Tauc profiles (b) of different samples prepared; PL spectrum (c), TRPL spectrum (d), transient photocurrent response (e) and EIS Nyquist diagram (f) of different samples; In situ XPS fine spectrum of Co 2p (g), O 1s (h) and S 2p (i) in CoF@CS@CO.

and holes was investigated using PL spectroscopy with an excitation wavelength of 420 nm (Fig. 5c). The PL spectrum peak value of CoF@Co_{1-x}S is 570 nm, which indicates a high probability of electron-hole recombination in CoF@Co_{1-x}S. When Co_{1-x}S nanosheets formed heterojunctions with Co₃O₄ nanowires, the PL spectra decreased significantly, indicating that the localized "electron sink" was realized due to the formation of MPBIEF, which led to the inhomogeneous dispersion of charge orientation on the surface of Co_{1-x}S nanosheets and induced the electron-hole separation [47].

The kinetics of electron-hole separation in the prepared photocatalyst was measured using time-resolved photoluminescence (TR-PL) spectroscopy, as shown in Fig. 5d. We used a biexponential decay function with the following expression to fit the decay curve of TR-PL (Eq. 3):

$$I(t) = A_1 \exp(-t/\tau_1) + A_2 \exp(-t/\tau_2) \quad (3)$$

The following relationship is used to calculate the mean life (τ_{ave}) (Eq. 4):

$$\tau_{ave} = \frac{\sum A_i \tau_i^2}{\sum A_i \tau_i} \quad (4)$$

Where, the τ represents emission lifetimes and A refers to the corresponding amplitude.

As shown in Table S1, the sample has two lifetimes τ_1 and τ_2 , where τ_1 corresponds to the recombination of surface-related charges and the recombination of free excitons. The mean τ_{ave} of CoF@Co_{1-x}S, CoF@Co₃O₄ and CoF@CS@CO were 2.723, 2.974 and 3.315 ns, respectively. The prolonged fluorescence lifetime indicates the presence of interfacial electron transfer, which is enhanced by excitation carrier transfer from Co_{1-x}S to Co₃O₄, with a significant reduction in the recombination of photogenerated electrons and holes [48].

The surface photovoltage (SPV) response signal is directly related to the number of electrons transferred during the photocatalytic process. The SPV response is caused by the band transition of the material. A simple diagram of the SPV test method is shown in Fig. S14. The top electrode is a blank FTO, connected to the amplifier, and a positive response indicates that the hole is transferred to the top electrode. Moreover, the negative response of SPV suggests that p-type CoF@Co₃O₄ is acquired. The positive reaction of SPV means that n-type CoF@Co_{1-x}S can be obtained. For single-phase materials, the photo-generated carriers are poorly separated in a specific wavelength range. In contrast, the peak intensity of the composite CoF@CS@CO

(maximum value of about 171.01 μV) was significantly higher than that of $\text{CoF@Co}_{1-x}\text{S}$ and $\text{CoF@Co}_3\text{O}_4$ (maximum values of about 50.77 μV and -46.76 μV , respectively), indicating that the formation of MPBIEF induces the accumulation of space charge at the contact interface and facilitates the rapid separation of photogenerated carriers [49]. Typically, the photocurrent response is used to reveal the photochemical properties of the photocatalyst surface. In this study, the transient photocurrent (i-t) curves of different samples were compared and the results are shown in Fig. 5e. The CoF@CS@CO composite exhibits the highest photocurrent density, which is much higher than that of the two monomer catalysts, indicating that the coupling of Co_{1-x}S nanosheets with multiple Co_3O_4 nanowires can significantly improve the carrier separation and transport rate [50]. Moreover, subtracting the recorded transient photocurrent density from the integral of the steady-state photocurrent with time yields a value proportional to the amount of positive charge deposited on the surface. Under the same conditions, the maximum surface charge density of CoF@CS@CO is 6.22 $\mu\text{C}/\text{cm}^2$, which is 4.20 times higher than that of Co_{1-x}S (1.48 $\mu\text{C}/\text{cm}^2$) and 3.82 times higher than that of Co_3O_4 (1.63 $\mu\text{C}/\text{cm}^2$) (Fig. S15). This result confirms that CoF@CS@CO has the largest region of space charge, suggesting that MPBIEF will be very helpful in facilitating charge separation and transfer at the interface [51]. The photostability of photocatalyst under light irradiation is of great significance for practical application. Noteworthy, the photostability of the composites can be evaluated by assessing the photocurrent stability under prolonged continuous light exposure. Fig. S16 shows the photocurrent density of CoF@CS@CO under 300 W xenon lamp illumination. The time-varying photocurrent results exhibit that the CoF@CS@CO photocatalytic material maintains a stable photocurrent of more than 0.97 $\mu\text{A}/\text{cm}^2$ after 500 min of continuous light irradiation, which has good photostability [52]. As shown in Fig. 5f, the fitting parameters derived from the inserted equivalent circuit are shown in Table S2. Among them, R_s and R_{ct} are the resistance of electrolyte solution and the interfacial carrier transfer resistance, and CPE is the constant-phase element (the test is

carried out under visible light irradiation). The CoF@CS@CO composite has the smallest radius of the arcs, which indicates that the charge transfer resistance is the least. This is mainly due to the fact that the surface charge of Co_{1-x}S nanosheets can be rapidly and directionally dispersed to multiple Co_3O_4 nanowires through the contact interface to form a local "electron sink", which hinders charge recombination. More specifically, the interface charge transfer resistances (R_{ct}) calculated for $\text{CoF@Co}_{1-x}\text{S}$, $\text{CoF@Co}_3\text{O}_4$ and CoF@CS@CO are 38.74, 30.46 and 23.42 Ω , respectively. Apparently, the charge transfer resistance of CoF@CS@CO is the smallest, indicating that MPBIEF promotes rapid charge transfer [53]. In order to more accurately demonstrate the catalyst surface charge transfer pathway of MPBIEF under light illumination, the in-situ XPS (IXPS) experiments were performed on CoF@CS@CO . As shown in Fig. 5g-i, the binding energy of the O 1s element in XPS under light conditions was positively shifted by 0.3 eV compared to that under darkness, while the binding energy of the S 2p element was negatively shifted by 0.3 eV relative to that under darkness, which suggests that the charge transfer pathway is from the surface of Co_3O_4 nanowires to the surface of Co_{1-x}S nanosheets under light conditions [54].

In order to understand the role of active substances in photocatalytic processes, tert-butanol (TBA), furfuryl alcohol (FFA), p-benzoquinone (p-BQ), disodium ethylenediaminetetraacetic acid (EDTA-2Na), and potassium bromate (PB) were selected as quenching agents for $\cdot\text{OH}$, $^1\text{O}_2$, $\text{O}_2^{\cdot-}$, h^+ , and e^- , respectively [55]. As shown in Fig. 6a, the catalytic performance is significantly decreased by the addition of EDTA-2Na and p-BQ, indicating that h^+ and $\text{O}_2^{\cdot-}$ are the most dominant species in the photocatalytic oxidation process of ENR. In addition, the degradation rate of ENR was inhibited when FFA was added, indicating that $^1\text{O}_2$ played a certain role in the system. The addition of PB also showed an inhibitory effect, which could be attributed to the decrease in $\text{O}_2^{\cdot-}$ generation due to electron capture by the quencher. In summary, h^+ and $\text{O}_2^{\cdot-}$ are the most important active substances in the catalytic oxidation process of ENR, followed by $^1\text{O}_2$. In the reduction of Cr(VI) ,

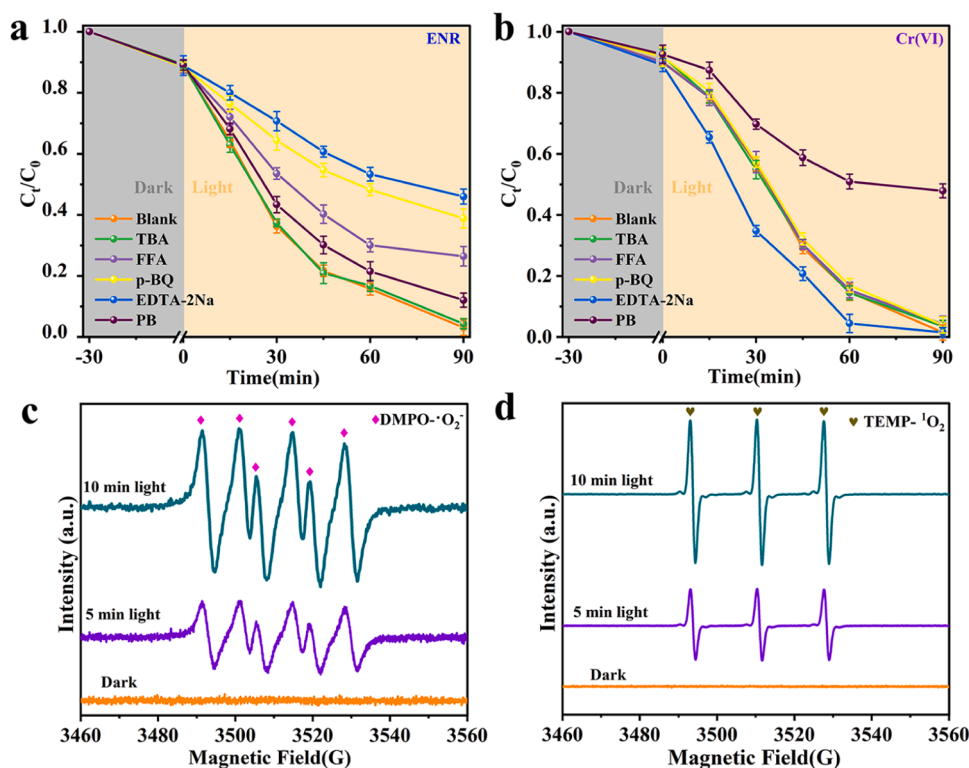


Fig. 6. The removal efficiency of ENR (a) and reduction efficiency of Cr(VI) (b) in the presence of different scavengers; EPR spectra of $\text{DMPO} \cdot \text{O}_2^{\cdot-}$ (c) and $\text{TEMP} \cdot ^1\text{O}_2$ (d).

the removal efficiency is improved by the addition of EDTA-2Na, while the reduction efficiency is significantly decreased with the inclusion of PB. This phenomenon shows that e^- is the only free radical in the reduction process of Cr(VI) (Fig. 6b). The apparent rate constant (k) in Fig. S17 provides a more intuitive understanding of the overall contribution of each active substance to ENR oxidation and Cr(VI) reduction in the CoF@CS@CO photocatalytic process. Electron paramagnetic resonance (EPR) technique is a powerful means of providing the most direct evidence for the identification of reactive species involved in photocatalytic processes, and in this study, the type of reactive oxygen species (ROS) of CoF@CS@CO is determined using DMPO and TEMP as spin trapping agents. No characteristic signal was found in the dark, but a four-element signal of DMPO- $O_2^{\cdot-}$ with a spin-derived number of 1:1:1:1 appeared under visible-light irradiation and was enhanced with irradiation time (Fig. 6c). A similar phenomenon was observed when dispersing CoF@CS@CO in water containing TEMP. Under visible light irradiation, the triplet signal of TEMP- 1O_2 was found to increase

significantly with the increase of illumination time, indicating that 1O_2 could be generated by a charge transfer process, which was consistent with the results of the capture experiments described above (Fig. 6d) [56].

Density Functional Theory (DFT) calculations intuitively reveal the interfacial interactions and charge transfer mechanisms of CoF@CS@CO photocatalysts. According to the previous SEM images, it is known that the $Co_{1-x}S$ nanosheet will contact with multiple Co_3O_4 nanowires to form a multi-parallel structure. Therefore, the $Co_{1-x}S$ planes combined with four Co_3O_4 nanowires are chosen in this study to simulate the real environment. As shown in Fig. 7a, the structural model of the combination of $Co_{1-x}S$ and Co_3O_4 is viewed from different angles. The density of states (DOS) of $Co_{1-x}S$ is analyzed in Fig. 7b. The valence band top VBM mainly contributes to the orbital of S, while the conduction band bottom CBM mainly contributes to the orbital component of Co. Notably, the DOS of Co_3O_4 indicates that the valence band maximum (VBM) mainly contributes to the orbital of Co and O, while the

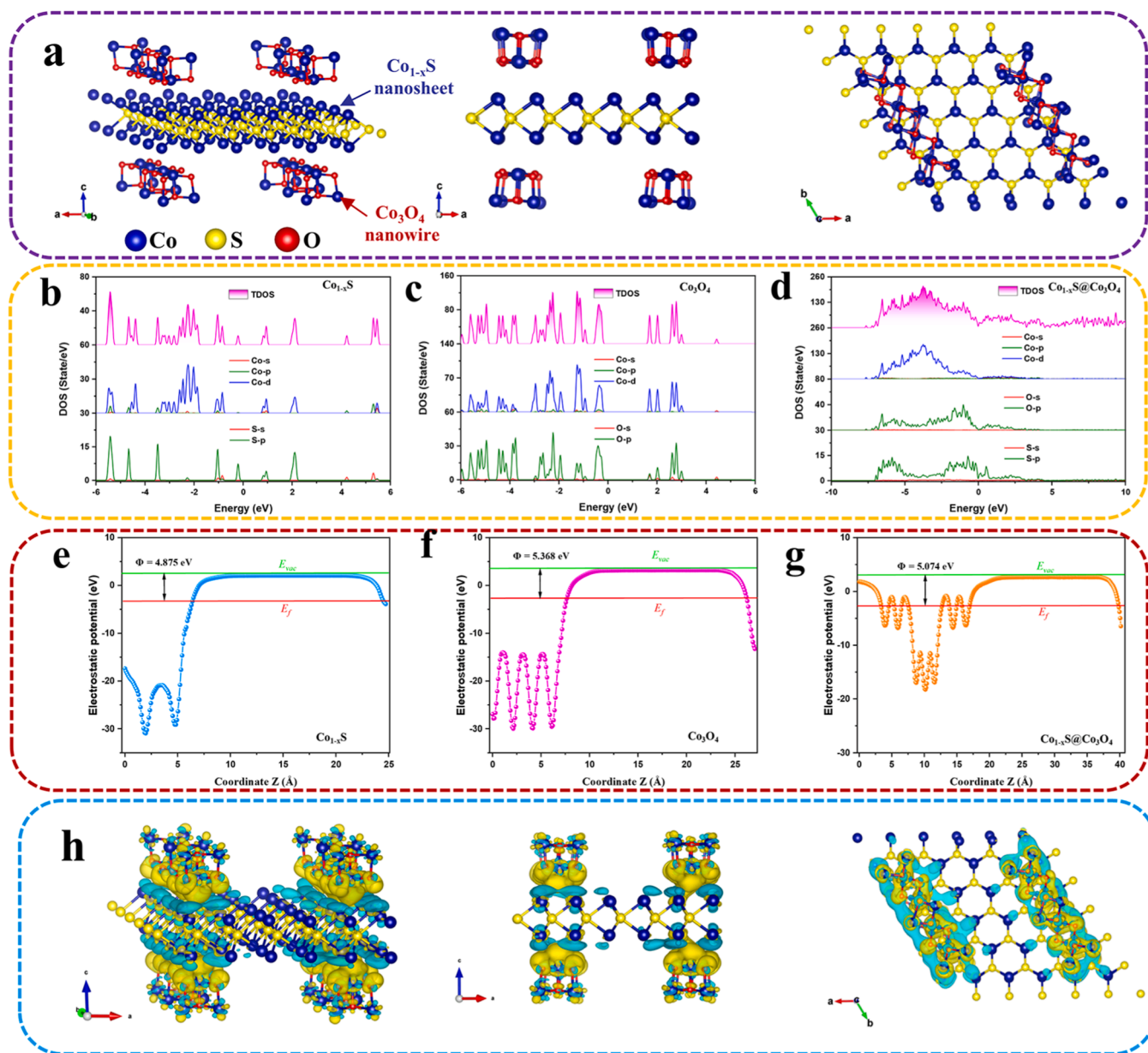


Fig. 7. Schematic of different orientations of the $Co_{1-x}S@Co_3O_4$ model used for DFT calculations (a); TDOS (b-d) and work function (e-g) of $Co_{1-x}S$, $Co_{1-x}S$ and $Co_{1-x}S@Co_3O_4$; Space charge distribution $Co_{1-x}S@Co_3O_4$ with different orientations to form multi-parallel built-in electric fields (MPBIEF) (h) (Remarks: model simulation SEM results each $Co_{1-x}S$ nanosheet will be in close contact with multiple Co_3O_4 nanowires).

conduction band minimum (CBM) mainly contributes to the orbital component of Co (Fig. 7c). In addition, the valence band top VBM of the composite-structured DOS is mainly contributed by the orbitals of Co and of O, while the conduction band bottom CBM is mainly contributed by the orbital components of Co (Fig. 7d). The band gap of the heterojunction reduces significantly after the composite, which on the one hand indicates the formation of the p-n heterojunction, and on the other hand similarly favors the contact surface charge transport [57]. Moreover, the electronic states all pass through the Fermi levels of the two spin components, indicating metallic features and enhanced conductivity. In summary, this interfacial enhancement mechanism accelerates the transfer rate of electrons and inhibits the complexation of interfacial e^- and h^+ . The Fermi level of the semiconductor is considered to be an important parameter for estimating the charge transport on the catalyst surface. The Fermi energy is given by the formula $\phi = E_{va} - E_f$. In addition, the electrostatic potential of $Co_{1-x}S$, Co_3O_4 and $Co_{1-x}S@Co_3O_4$ is shown in Fig. 7e-g, and their calculated work functions are 4.875 eV, 5.368 eV, and 5.074 eV, respectively. The Fermi level of $Co_{1-x}S$ is 2.101 eV, which is lower than that of Co_3O_4 (3.237 eV), which can drive the charge transfer from $Co_{1-x}S$ to Co_3O_4 until the Fermi level reaches equilibrium. After reaching the Fermi equilibrium, a space charge region with a strong internal electric field can be formed, thus effectively promoting the separation of photo-generated carriers in the photocatalytic reaction [58]. The spatial charge distribution diagram in Fig. 7h shows the charge transfer from the

$Co_{1-x}S$ interface to Co_3O_4 at different angles. According to Fermi level calculation, the $Co_{1-x}S$ nanosheets can act as electron "pump" to spontaneously transfer charges to multiple Co_3O_4 nanowires, forming multi-parallel built-in electric fields (MPBIEF). The parallel distribution of MPBIEF along the $Co_{1-x}S$ plane causes the $Co_{1-x}S$ surface charge to be distributed asymmetrically at the interface in contact with Co_3O_4 , resulting in the formation of a localized "electron sink". This unique structure can promote the directional asymmetric dispersive motion of carriers under light conditions, resulting in efficient separation and migration of carriers. In addition, as shown in the enlarged differential charge distribution diagram in Fig. S18, the charge accumulation region is mainly concentrated on the O atom of Co_3O_4 (yellow part), and the charge consumption area is mainly concentrated on the Co atom of $Co_{1-x}S$ (blue part), thus the overall charge is transferred from $Co_{1-x}S$ to Co_3O_4 . Moreover, the calculated Bader charges are shown in Table S3, with a total charge of 1560 eV, 864 eV for $Co_{1-x}S$ monomer and 696 eV for Co_3O_4 . In the heterojunction system, the charge amount of $Co_{1-x}S$ is 852.5505 eV, and that of Co_3O_4 is 707.4496 eV. Therefore, the amount of charge transfer is $864 - 852.5505 \text{ eV} = 11.4495 \text{ eV}$ from $Co_{1-x}S$ to Co_3O_4 . Bader analysis shows that Co atoms mainly act as electron donors and O atoms mainly act as electron acceptors, which is consistent with the results of the charge density difference. These results indicate that the Co atoms from $Co_{1-x}S$ and the O atoms from Co_3O_4 in the heterojunction system affect the characteristics of the built-in electric field through charge migration.

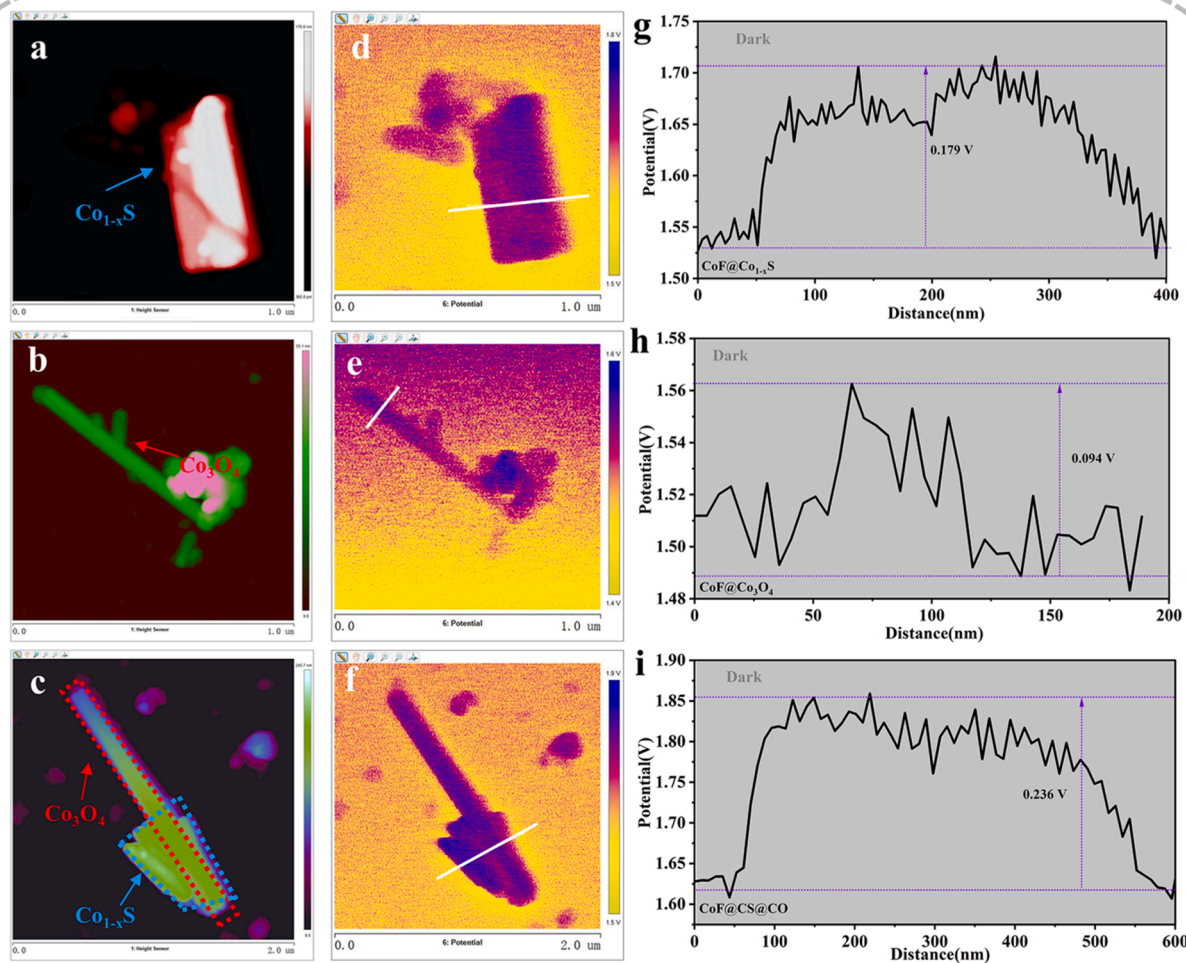


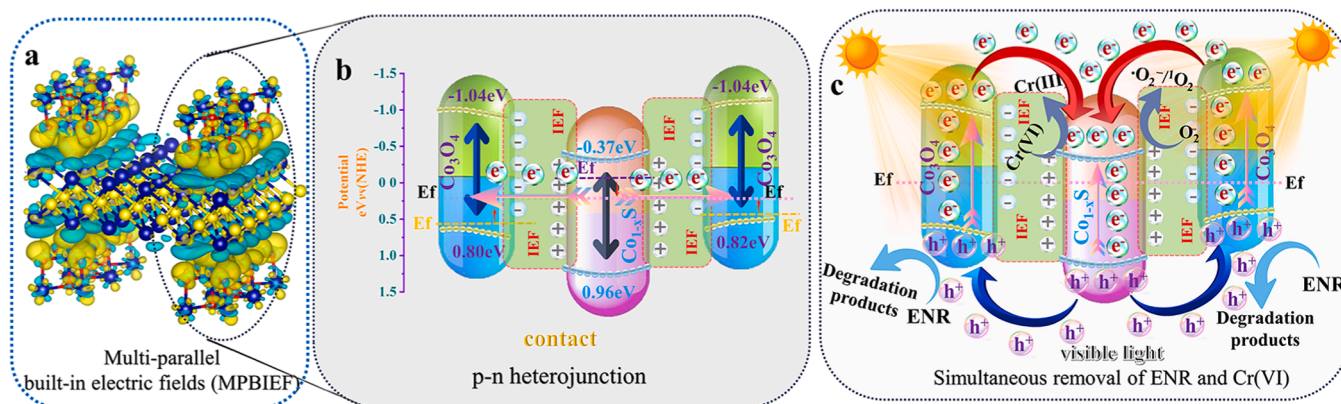
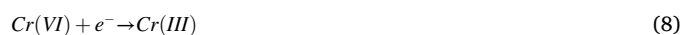
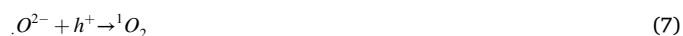
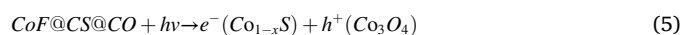
Fig. 8. KPFM morphology of $CoF@Co_{1-x}S$ (a), $CoF@Co_3O_4$ (b), and $CoF@CS@CO$ (c); KPFM potentiogram of $CoF@Co_{1-x}S$ (d), $CoF@Co_3O_4$ (e), and $CoF@CS@CO$ (f); The corresponding surface potential of $CoF@Co_{1-x}S$ (g), $CoF@Co_3O_4$ (h), and $CoF@CS@CO$ (i) (Experimental condition: in the dark).

In-situ light irradiation electron paramagnetic resonance (EPR) spectroscopy was used to observe the concentration of photoexcited electrons. Under both light irradiation and dark conditions, the integrated area of the EPR signal of the CoF@CS@CO composite is much larger than that of the two monomers, indicating a higher concentration of photoexcited electrons (Fig. S19). This result shows that the carrier generated by light excitation can be directionally dispersed due to the presence of MPBIEF, which reduces the recombination probability [59]. To gain insight into the separation of interfacial charges between Co_{1-x}S and Co₃O₄, the researchers used Kelvin probe Force microscopy (KPFM) in combination with a photosystem to visualize changes in surface potentials under dark and light conditions. The morphologies of CoF@Co_{1-x}S, CoF@Co₃O₄ and CoF@CS@CO are shown in Fig. 8a-c. CoF@Co_{1-x}S and CoF@Co₃O₄ are 2D nanosheets and 1D nanowires structures, respectively, whereas the composite CoF@CS@CO retains the morphology of both, which is consistent with the results of the TEM tests (the structure is partially disrupted due to the sample being lightly scraped directly from the foam metal surface). Fig. 8d-f shows the average contact potential difference (ACPD) under dark conditions in the regions where the three samples mentioned above are located. As shown in Fig. 8g-i, the average surface potential (SP) of the CoF@CS@CO composites characterized by KPFM turns out to be 0.236 V, which is significantly higher than that of 0.179 V and 0.094 V for the CoF@Co_{1-x}S and CoF@Co₃O₄ samples. The increase of SP indicates the apparent formation of a localized internal electric field at the interface of Co_{1-x}S and Co₃O₄, which leads to a better separation of light-generated electrons and holes, in agreement with the results of DFT calculation [60]. Under light illumination, the SP of CoF@CS@CO rises to 0.251 V, as shown in Fig. S20. The large difference between the surface potential of the composites in dark and light indicates that the presence of the internal electric field promotes and activates the directional movement of photogenerated carriers and facilitates the convergence of strong electrons at the interface of the Co_{1-x}S and Co₃O₄ contacts [61].

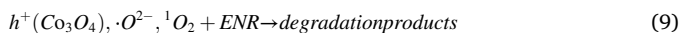
Based on the above experimental and calculation results, the electron transfer mechanism of p-n heterojunction induced by multi-parallel built-in electric fields (MPBIEF) is proposed. The photocatalytic mechanism of the heterojunction consisting of Co_{1-x}S nanosheets and Co₃O₄ nanowires for simultaneous degradation of ENR and reduction of Cr(VI) is shown in Scheme 2. One Co_{1-x}S nanosheet is seen to be in contact with multiple Co₃O₄ nanowires by SEM image. According to DFT and flat band potential, the Fermi level of n-type Co_{1-x}S semiconductor is lower than that of p-type Co₃O₄ semiconductor. Upon contact, Co_{1-x}S acts as an electron "pump" to transfer the negative charge to Co₃O₄ until the Fermi levels of Co_{1-x}S and Co₃O₄ are aligned, forming several typical p-n Co_{1-x}S/Co₃O₄ junctions in the Co_{1-x}S plane [62]. As a result of the charge redistribution, multiple MPBIEF are formed in the space charge region, which results in a non-uniform distribution of charge

across the Co_{1-x}S nanosheet plane. This unique charge distribution structure is shown in Scheme 2a, where the inhomogeneous charge distribution of Co_{1-x}S nanosheets forms multiple "electron sinks" that serve as pathways for the directional migration of subsequent photo-generated charge carriers. By magnifying the Co_{1-x}S/Co₃O₄ contact interface, it can be seen that the downward-displaced band edge of Fermi level in the n-type Co_{1-x}S semiconductor bends upward after reaching equilibrium, while the upward-displaced band edge of Fermi level in the p-type Co₃O₄ semiconductor bends downward (Scheme 2b) [63]. The mechanism of e⁻ and h⁺ transfer under light and photocatalytic degradation of ENR and reduction of Cr(VI) are shown in Scheme 2c. Firstly, Co_{1-x}S and Co₃O₄ are activated under visible light, inducing the transfer of e⁻ from VB to CB, leaving photogenerated h⁺ in VB. Then, under the combined effect of multiple parallel internal electric fields and band-edge bending, photoelectrons generated on the CB of multiple Co₃O₄ nanowires rapidly migrate to the CB of the contacting Co_{1-x}S nanosheets, and the h⁺ on the VB of the Co_{1-x}S nanosheets migrate to the VB of the Co₃O₄ nanowires in parallel. This directional migration of photogenerated carriers toward the formation of "electron sinks" unevenly disperses the charge on the Co_{1-x}S plane and hinders the contact probability of e⁻ and h⁺ on the Co_{1-x}S plane. Since the CB potential of Co_{1-x}S, -0.37 eV, is lower than the O²⁻/O₂ potential (-0.33 eV vs NHE) and Cr(VI)/Cr(III) potential (0.51 eV vs NHE, pH = 6.8), the adsorbed O₂ and Cr(VI) will definitely produce O²⁻ and Cr(III) when combining electrons, whereas the h⁺ of Co₃O₄ directly participates in the degradation reaction but cannot form ·OH (1.99 eV vs NHE). In addition, the VB edge potential of Co₃O₄ (0.82 V vs NHE) is higher than the standard REDOX potential of O²⁻/·O₂ (0.34 V vs NHE), indicating that O²⁻ binds h⁺ to form ¹O₂ [64]. Therefore, in the p-n heterojunction constructed by MPBIEF, the photogenerated carriers at the Co_{1-x}S/Co₃O₄ interface move directionally along the "electron sink" to realize the inhomogeneous dispersion of charges in the Co_{1-x}S plane, which dramatically reduces the recombination loss and achieves the spatial separation of photogenerated electron-hole pairs to prolong the lifetime of carriers, thus improving the photocatalytic performance.

Based on the above results and discussions, the present study hypothesized the following mechanism for the photocatalytic simultaneous degradation of ENR and reduction of Cr(VI) by CoF@CS@CO composites:



Scheme 2. Mechanism of simultaneous degradation of ENR and reduction of Cr(VI) by photocatalysis induced by multi-parallel built-in electric fields (MPBIEF).



3.6. ENR degradation pathway

Based on LC-MS analysis, 12 intermediates were identified during the degradation reaction (Fig. S21). Table S4 lists the possible intermediates. Based on the intermediates produced and previous studies, three degradation pathways were derived. As shown in Fig. 9a, the main reactions include 1) defluorination, 2) N-C bond cleavage between the quinolone and piperazine rings, 3) side chain oxidation of piperazine rings, 4) cyclopropane cleavage, and 5) quinolone decarboxylation [65]. In Pathway I, a h^+ attacks the piperazine ring, breaking the N-C bond to form E1 and E2. Deamination leads to the formation of E3, which is followed by cleavage and oxidation reactions to produce smaller molecules of E4 through both free radical and non-free radical initiated pathways. In Pathway II, defluorination produces E5 as the first intermediate. The piperazine ring is oxidized and ring-opened to form E6, and the quinolone group is decarboxylated to form E7. Additionally, cleavage, oxidation, and de-cyclopropane reactions of quinolone groups result in the formation of E8. In Pathway III, decarboxylation of the carboxyl group of the quinolone moiety occurs to form E9. Subsequently, attack of the piperazine ring by various active species, N-C bond breaking, and deamination reactions generate E10 and E11. As the reaction proceeds, smaller intermediate, E12, is formed. Eventually, smaller molecules, such as E4, E8 and E12, are mineralized into carbon dioxide and water.

ENR and its degradation intermediates were evaluated toxicologically using the toxicity assessment software tool (T.E.S.T.) based on the quantitative structure-activity relationship (QSAR) method [66]. As shown in Fig. 9b, the substance is considered to be "very toxic" when the LD₅₀ for feather minnow reaches 0.90 mg/L. After 96 h, the lethal concentration of ENR to minnows was only 0.16 mg/L. With the exception of E1, the LC₅₀ values of degradation intermediates are elevated relative to ENR, and E8 is considered "not harmful". As can be seen from Fig. 9c, ENR and its intermediates are within the concentration range of bioaccumulation factors. Nevertheless, most of the intermediates exhibited reduced bioaccumulation factor values compared to ENR. This suggests that the photocatalysis technology based on

CoF@CS@CO can effectively protect advanced consumers in the ecosystem. The developmental toxicity of ENR is expected to be reduced after photocatalytic treatment. In addition, 11 of the 12 intermediates were less developmental toxicity than ENR, and only the product E5 was slightly more toxic than ENR (Fig. 9d). Typically, the product E8 was predicted to be developmentally non-toxic. Finally, ENR was "mutagenic-positive", but the mutagenicity of all degradation products was reduced (Fig. 9e). Moreover, all intermediates are predicted to be "mutagenic negative" except E5, E8 and E9. Based on the predicted values of the above indexes, this study predicted that the biotoxicity of the ENR-containing solution would be reduced after photocatalytic treatment. After 90 min of visible light irradiation, the TOC removal rate of CoF@CS@CO was measured to be 58.9%, indicating that the ENR was partially mineralized to carbon dioxide and water (Fig. S22). These results further demonstrate the effectiveness of the CoF@CS@CO photocatalyst in degrading ENR under visible light conditions and reducing its water toxicity and TOC residue rate.

3.7. Simulation of realistic environments in practical applications

To further explore the potential value of CoF@CS@CO in practical applications, a fixed-bed photocatalytic reactor device was designed to simulate the actual wastewater treatment process. Digital images show that the appearance of CoF@CS@CO is an overall dark color, indicating the uniform in-situ growth of Co_{1-x}S and Co₃O₄ on the Co-F surface (Fig. S23a). Fig. S23b shows the highly porous structure of CoF@CS@CO (porosity > 98%), the unique structure that avoids the blockage of effluent and light. As shown in Fig. 10a, the complete fixed-bed photocatalytic reactor unit consists of a contamination area, a peristaltic pump, a light source, a reactor and a collection zone. Fig. 10b shows a photograph of the reactor in operation. Real sewage systems are complex and contain not only various cations and ions, but also ammonia nitrogen, phosphate compounds and microorganisms. Therefore, it is necessary to explore the photocatalytic performance of the reactor under different water quality conditions. In this study, a stock solution of pollutants containing ENR and Cr(VI) was prepared using deionized water, tap water and river water as solvents, and then the flow-through removal efficiency was tested using a fixed-bed

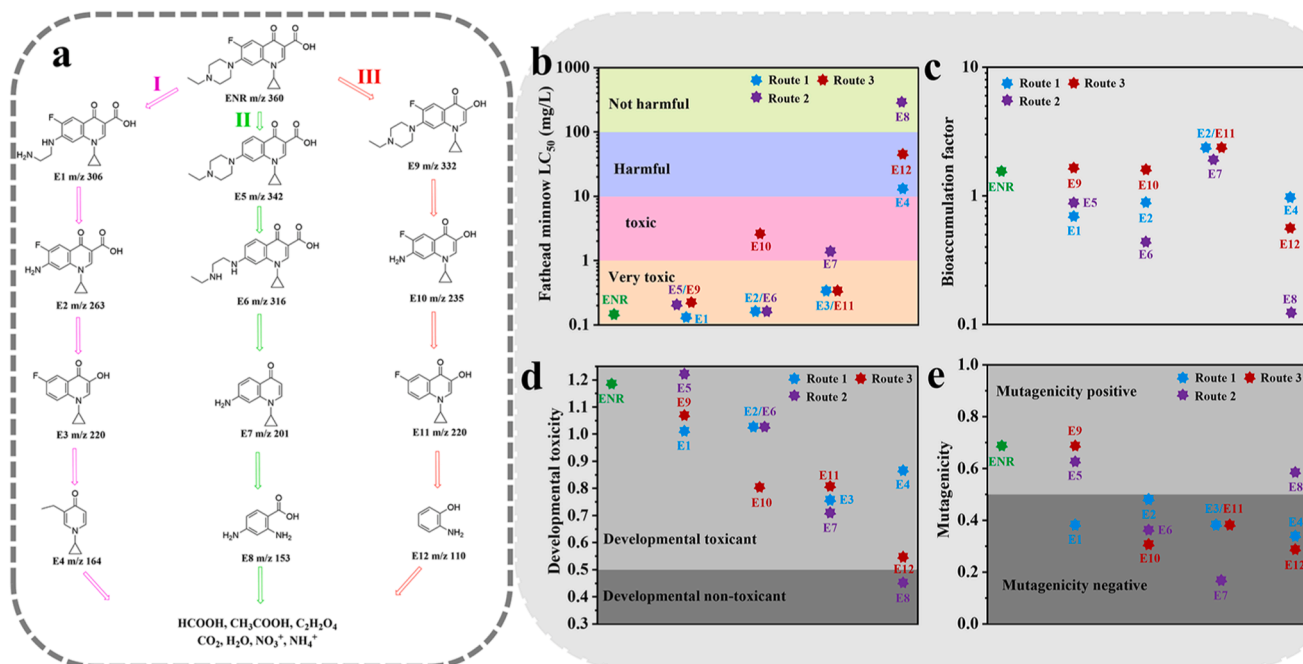


Fig. 9. CoF@CS@CO photocatalytic degradation of ENR(a); QSAR analysis based on fathead minnow LC₅₀ (96 hr) (b), bioaccumulation factors (c), developmental toxicity (d), and mutagenicity (e).

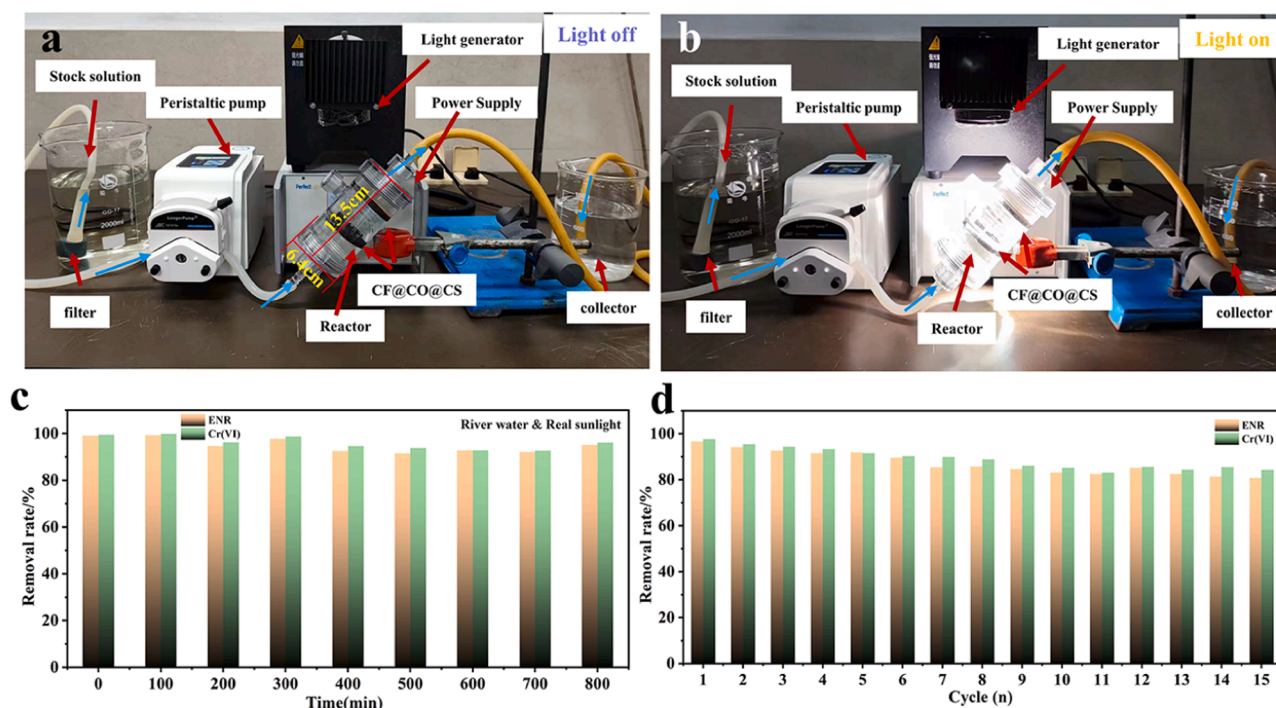


Fig. 10. Structure diagram of the fixed-bed photocatalytic flow treatment unit in the dark (a) and with the light on (b); Removal efficiency (c) and cycling performance (d) of ENR and Cr(VI) in visible light and river water systems.

photocatalytic reaction unit. The initial concentrations of ENR and Cr(VI) in the coexisting solutions were both $10 \text{ mg} \cdot \text{L}^{-1}$, and the experimental results are shown in Fig. S24. However, after 400 min of continuous operation, the fixed-bed photocatalytic flow-through treatment unit was slightly weaker than the other three systems in removing ENR and Cr(VI) under riverine conditions (flow rate of $5 \text{ mL} \cdot \text{min}^{-1}$, HRT of 87 min). Therefore, the actual water quality is more complex with different physical parameters and chemical composition, which affects the effectiveness of ENR and Cr(VI) removal. A solar light source will be the final and best energy option for the operation of the photocatalytic system. Real sunlight is utilized as a light source to remove the simulated wastewater solution in a river water configuration, and the operation performance of the reactor has been verified in a real environment. After 800 min of continuous operation in a simulated real environment, the removal efficiency of ENR and Cr(VI) reached 95.12% and 96.13%, respectively (Fig. 10c). The continuous operation performance, maneuverability and stability of the reactor determine its practical application value. Therefore, this study conducted 15 cycle tests on the reactor, flushing the reactor three times with deionized water after each cycle. As shown in Fig. 10d, after 15 consecutive times of reactor operation, the removal efficiency only decreased by about 15% and remained above 80%. Moreover, a high TOC removal rate is still maintained during continuous operation (Fig. S25). The results show that the reactor based on CoF@CS@CO has good continuous operation performance and chemical stability, and has good application prospects in the field of photocatalytic removal of polluted solutions containing ENR and Cr(VI) [67].

4. Conclusions

In summary, the in-situ growth of Co_{1-x}S nanosheets and Co_3O_4 nanowires on the CoF surface addresses the challenges related to the recovery of powdered catalysts and the stability of supported catalysts developed on inert substrates (e.g., carbon felt, sponge). SEM analysis confirms that Co_{1-x}S nanosheets are tightly connected to multiple Co_3O_4 nanowires, while theoretical calculations reveal the formation of multi-

parallel built-in electric fields (MPBIEF). This internal electric field parallel to the Co_{1-x}S plane causes the surface charge of Co_{1-x}S to be asymmetrically distributed at the interface in contact with Co_3O_4 , resulting in the formation of a localized "electron sink". This unique structure promotes the directional asymmetric dispersion of charge carriers under light conditions, reducing the likelihood of electron-hole recombination. KPFM experiments demonstrate that the presence of an internal electric field enhances and activates the directional movement of photogenerated carriers. Consequently, the designed CoF@CS@CO catalyst is capable of simultaneous degradation of ENR and reduction of Cr(VI), exhibiting a synergistic effect in the case of coexistence of the two pollutants. The fixed-bed photocatalytic flow treatment device constructed based on CoF@CS@CO photocatalyst achieves the removal of complex pollutants from river water under sunlight, demonstrating its application potential. This study elucidates the role of MPBIEF in heterojunctions, providing a theoretical and practical foundation for generating and interpreting related studies.

CRediT authorship contribution statement

Hu Yongyou: Writing – review & editing, Methodology. **Cheng Jianhua:** Funding acquisition. **Lin Jialiang:** Software, Resources. **Niu Jiliang:** Writing – original draft, Formal analysis, Data curation, Conceptualization.

Declaration of Competing Interest

The authors declare that they have no known competing financial interests or personal relationships that could have appeared to influence the work reported in this paper.

Data availability

No data was used for the research described in the article.

Acknowledgement

This work was financed by National Natural Science Foundation of China (No. 21976060).

Appendix A. Supporting information

Supplementary data associated with this article can be found in the online version at doi:10.1016/j.apcatb.2024.123825.

References

- [1] L. Sun, Y. Feng, K. Ma, X. Jiang, Z. Gao, J. Wang, N. Jiang, X. Liu, Synergistic effect of single-atom Ag and hierarchical tremella-like g-C₃N₄: electronic structure regulation and multi-channel carriers transport for boosting photocatalytic performance, *Appl. Catal. B Environ.* 306 (2022), <https://doi.org/10.1016/j.apcatb.2022.121106>.
- [2] N.A. Nordin, M.A. Mohamed, M.N.I. Salehmin, S.F. Mohd Yusoff, Photocatalytic active metal-organic framework and its derivatives for solar-driven environmental remediation and renewable energy, *Coord. Chem. Rev.* 468 (2022), <https://doi.org/10.1016/j.ccr.2022.214639>.
- [3] F. Chen, G.X. Huang, F.B. Yao, Q. Yang, Y.M. Zheng, Q.B. Zhao, H.Q. Yu, Catalytic degradation of ciprofloxacin by a visible-light-assisted peroxymonosulfate activation system: performance and mechanism, *Water Res.* 173 (2020) 115559, <https://doi.org/10.1016/j.watres.2020.115559>.
- [4] M. Han, Y. Chen, J. Li, Y. Dong, Z. Miao, J. Li, L. Zhang, Effects of organic chromium sources on growth performance, lipid metabolism, antioxidant status, breast amino acid and fatty acid profiles in broilers, *J. Sci. Food Agric.* 101 (9) (2021) 3917–3926, <https://doi.org/10.1002/jsfa.11053>.
- [5] Y. Liang, W. Xu, J. Fang, Z. Liu, D. Chen, T. Pan, Y. Yu, Z. Fang, Highly dispersed bismuth oxide quantum dots/graphite carbon nitride nanosheets heterojunctions for visible light photocatalytic redox degradation of environmental pollutants, *Appl. Catal. B Environ.* 295 (2021), <https://doi.org/10.1016/j.apcatb.2021.120279>.
- [6] J. Niu, Y. Peng, T. Hu, Y. Chen, J. Cheng, Y. Hu, Development of interfacial strong Interaction-enhanced C-F@CuBi₂(Ox/Ni-x)/4/CN Nano-sheet clusters photocatalysts for the simultaneous degradation of tetracycline and reduced Cr (VI), *Chem. Eng. J.* 454 (2023), <https://doi.org/10.1016/j.cej.2022.140203>.
- [7] S. Chen, B. Li, D. Huang, P. Xu, Y. Chen, L. Lei, Z. Wang, R. Deng, L. Du, G. Wang, Jointed synchronous photocatalytic oxidation and chromate reduction enabled by the defect distribution upon BiVO₄(4): mechanism insight and toxicity assessment, *ACS Appl. Mater. Interfaces* 13 (15) (2021) 17586–17598, <https://doi.org/10.1021/acsami.1c01998>.
- [8] L. Zhang, J. Zhang, H. Yu, J. Yu, Emerging S-scheme photocatalyst, *Adv. Mater.* 34 (11) (2022) e2107668, <https://doi.org/10.1002/adma.202107668>.
- [9] J. Niu, R. Hu, L. Tang, Y. Huang, J. Cheng, Y. Hu, In-situ growth of C-F@CCS@ZIF8/67–1/1 photocatalysts with internal electric field and interfacial enhancement on cobalt-copper foam surface for simultaneous removal of ciprofloxacin and Cr(VI), *Appl. Catal. B Environ.* 334 (2023), <https://doi.org/10.1016/j.apcatb.2023.122857>.
- [10] J. Zheng, Z. Lei, Incorporation of CoO nanoparticles in 3D marigold flower-like hierarchical architecture MnCo₂O₄ for highly boosting solar light photo-oxidation and reduction ability, *Appl. Catal. B Environ.* 237 (2018) 1–8, <https://doi.org/10.1016/j.apcatb.2018.05.060>.
- [11] X.L. Wu, S. Liu, Y. Li, M. Yan, H. Lin, J. Chen, S. Liu, S. Wang, X. Duan, Directional and ultrafast charge transfer in oxygen-vacancy-rich ZnO@single-atom cobalt core-shell junction for photo-fenton-like reaction, *Angew. Chem. Int. Ed. Engl.* 62 (30) (2023) e202305639, <https://doi.org/10.1002/anie.202305639>.
- [12] M. Zhang, L. Tang, Y. Zhu, Y. Zhang, J. Liu, J. Wang, C. Feng, L. Qiao, Y. Chen, Conjugated polymers S-scheme homojunction with large internal electric field and matching interface for efficient visible light photocatalytic degradation of ciprofloxacin, *J. Clean. Prod.* 419 (2023), <https://doi.org/10.1016/j.jclepro.2023.138199>.
- [13] J. Zhang, X. Tan, L. Shi, H. Chen, Y. Liu, S. Wang, X. Duan, M. Wu, H. Sun, S. Wang, Tandem internal electric fields in intralayer/interlayer carbon nitride homojunction with a directed flow of photo-excited electrons for photocatalysis, *Appl. Catal. B Environ.* 333 (2023), <https://doi.org/10.1016/j.apcatb.2023.122781>.
- [14] W. Jiang, H. Zhu, J. Yang, B.Q.L. Low, W.Y. Wu, M. Chen, J. Ma, R. Long, J. Low, H. Zhu, J.Z.X. Heng, K.Y. Tang, C.H.T. Chai, M. Lin, Q. Zhu, Y.W. Zhang, D. Chi, Z. Li, X.J. Loh, Y. Xiong, E. Ye, Integration of single-atom catalyst with Z-scheme heterojunction for cascade charge transfer enabling highly efficient Piezo-photocatalysis, *Adv. Sci.* 10 (28) (2023) e2303448, <https://doi.org/10.1002/advs.202303448>.
- [15] J. Niu, T. Hu, Y. Chen, J. Cheng, X. Zhou, Y. Hu, Construction of F-F@FeVO₄/ZnCo₂O₄ photocatalysts with heterojunction interfacial enhancement and surface oxygen vacancies for the removal of tetracycline, sulfamethoxazole, ciprofloxacin and Cr(VI), *J. Clean. Prod.* 397 (2023), <https://doi.org/10.1016/j.jclepro.2023.136601>.
- [16] Z. Chen, X. Li, Y. Wu, J. Zheng, P. Peng, X. Zhang, A. Duan, D. Wang, Q. Yang, S-scheme Cs₂AgBiBr₆/Ag₃PO₄ heterojunction with efficient photocatalysis performance for H₂ production and organic pollutant degradation under visible light, *Sep. Purif. Technol.* 295 (2022), <https://doi.org/10.1016/j.seppur.2022.121250>.
- [17] L. Wang, G. Tang, S. Liu, H. Dong, Q. Liu, J. Sun, H. Tang, Interfacial active-site-rich 0D Co₃O₄/1D TiO₂ p-n heterojunction for enhanced photocatalytic hydrogen evolution, *Chem. Eng. J.* 428 (2022), <https://doi.org/10.1016/j.cej.2021.131338>.
- [18] M. Gao, J. Fan, X. Li, Q. Wang, D. Li, J. Feng, X. Duan, A carbon-negative hydrogen production strategy: CO(2) selective capture with H(2) production, *Angew. Chem. Int. Ed. Engl.* 62 (15) (2023) e202216527, <https://doi.org/10.1002/anie.202216527>.
- [19] Y. Ti, F. Tian, Q. Zhang, L. Gai, S. Liu, Q. Shen, Introduction of as-prepared cobalt source-containing carbon nanotubes to Co1-S@C mesoporous nanospheres for an ultrahigh lithium storage, *Carbon* 165 (2020) 112–121, <https://doi.org/10.1016/j.carbon.2020.04.042>.
- [20] F. Yang, K. Sliozberg, I. Sinev, H. Antoni, A. Bahr, K. Ollegott, W. Xia, J. Masa, W. Grunert, B.R. Cuenya, W. Schuhmann, M. Muhler, Synergistic effect of cobalt and iron in layered double hydroxide catalysts for the oxygen evolution reaction, *ChemSusChem* 10 (1) (2017) 156–165, <https://doi.org/10.1002/cssc.201601272>.
- [21] J. Lv, L. Wang, R. Li, K. Zhang, D. Zhao, Y. Li, X. Li, X. Huang, G. Wang, Constructing a hetero-interface composed of oxygen vacancy-enriched Co₃O₄ and crystalline-amorphous NiFe-LDH for oxygen evolution reaction, *ACS Catal.* 11 (23) (2021) 14338–14351, <https://doi.org/10.1021/acscatal.1c03960>.
- [22] W. Zhang, K. Lassen, C. Descorme, J.L. Valverde, A. Giroir-Fendler, Effect of the precipitation pH on the characteristics and performance of Co₃O₄ catalysts in the total oxidation of toluene and propane, *Appl. Catal. B Environ.* 282 (2021), <https://doi.org/10.1016/j.apcatb.2020.119566>.
- [23] J. Lu, S. Zhang, Z. Miao, Y. Yin, C. Ma, X. Liu, J. Wang, W. Qiao, L. Ling, Functional interlayer with highly dispersed Co1-XS embedded in N-doped carbon spheres as trapping-catalyst nanoreactors for advanced lithium-sulfur batteries, *ACS Appl. Energy Mater.* 6 (9) (2023) 4724–4733, <https://doi.org/10.1021/acsami.3c00075>.
- [24] Y. Zhang, Y. Sun, Y. Man, X. Jiang, R. Zhao, G. Xiang, L. He, Construction of a controllable and dispersed Fe₃O₄-based catalyst using ZIFs as a spatial support for highly catalytic degradation of aflatoxin B₁, *Appl. Catal. B Environ.* 318 (2022), <https://doi.org/10.1016/j.apcatb.2022.121818>.
- [25] D. Guo, J. Wang, L. Zhang, X. Chen, Z. Wan, B. Xi, Strategic atomic layer deposition and electrospinning of cobalt sulfide/nitride composite as efficient bifunctional electrocatalysts for overall water splitting, *Small* 16 (35) (2020) e2002432, <https://doi.org/10.1002/sml.202002432>.
- [26] G. Zhao, G. Hai, P. Zhou, Z. Liu, Y. Zhang, B. Peng, W. Xia, X. Huang, G. Wang, Electrochemical oxidation of 5-hydroxymethylfurfural on CeO₂-modified Co₃O₄ with regulated intermediate adsorption and promoted charge transfer, *Adv. Funct. Mater.* 33 (14) (2023), <https://doi.org/10.1002/adfm.202213170>.
- [27] Z. Wang, S. Chen, L. Wang, S. Gao, M. Li, H. Li, Y. Zhu, E. Shangguan, Microwave-anion-exchange route to spinel CuCo₂S₄ nanosheets as cathode materials for magnesium storage, *J. Power Sources* 556 (2023), <https://doi.org/10.1016/j.jpowsour.2022.232480>.
- [28] M. Sahoo, S. Mansingh, K.M. Parida, A bimetallic Au–Ag nanoalloy mounted LDH/RGO nanocomposite: a promising catalyst effective towards a coupled system for the photoredox reactions converting benzyl alcohol to benzaldehyde and nitrobenzene to aniline under visible light, *J. Mater. Chem. A* 7 (13) (2019) 7614–7627, <https://doi.org/10.1039/c8ta10521a>.
- [29] Ö. Tuna, Z. Balta, E.B. Simsek, Quantum sized engineering of FeTiO₃ perovskite for enhanced photocatalytic mineralization of antibiotics: comprehensive exploration of roles of NCQDs and BNQDs in charge transfer dynamics, *Chem. Eng. J.* 474 (2023), <https://doi.org/10.1016/j.cej.2023.145770>.
- [30] X. Tang, Y. Huang, Q. He, Y. Wang, H. Zheng, Y. Hu, Adsorption of tetracycline antibiotics by nitrilotriacetic acid modified magnetic chitosan-based microspheres from aqueous solutions, *Environ. Technol. Innov.* 24 (2021), <https://doi.org/10.1016/j.eti.2021.101895>.
- [31] F. Zhao, Y. Liu, S.B. Hammouda, B. Doshi, N. Guizarro, X. Min, C.-J. Tang, M. Sillanpää, K. Sivula, S. Wang, MIL-101(Fe)/g-C₃N₄ for enhanced visible-light-driven photocatalysis toward simultaneous reduction of Cr(VI) and oxidation of bisphenol A in aqueous media, *Appl. Catal. B Environ.* 272 (2020), <https://doi.org/10.1016/j.apcatb.2020.119033>.
- [32] J. Huang, D. Li, R. Li, P. Chen, Q. Zhang, H. Liu, W. Lv, G. Liu, Y. Feng, One-step synthesis of phosphorus/oxygen co-doped g-C(3)N(4)/anatase TiO(2) Z-scheme photocatalyst for significantly enhanced visible-light photocatalysis degradation of enrofloxacin, *J. Hazard. Mater.* 386 (2020) 121634, <https://doi.org/10.1016/j.jhazmat.2019.121634>.
- [33] Y. Wang, L. Rao, P. Wang, Z. Shi, L. Zhang, Photocatalytic activity of N-TiO₂/O-doped N vacancy g-C₃N₄ and the intermediates toxicity evaluation under tetracycline hydrochloride and Cr(VI) coexistence environment, *Appl. Catal. B Environ.* 262 (2020), <https://doi.org/10.1016/j.apcatb.2019.118308>.
- [34] W. Wang, Q. Niu, G. Zeng, C. Zhang, D. Huang, B. Shao, C. Zhou, Y. Yang, Y. Liu, H. Guo, W. Xiong, L. Lei, S. Liu, H. Yi, S. Chen, X. Tang, 1D porous tubular g-C₃N₄ capture black phosphorus quantum dots as 1D/0D metal-free photocatalysts for oxytetracycline hydrochloride degradation and hexavalent chromium reduction, *Appl. Catal. B Environ.* 273 (2020), <https://doi.org/10.1016/j.apcatb.2020.119051>.
- [35] J. Zhong, T. Ni, J. Huang, D. Li, C. Tan, Y. Liu, P. Chen, C. Wen, H. Liu, Z. Wang, W. Lv, G. Liu, Directional utilization disorder charge via In-plane driving force of functionalized graphite carbon nitride for the robust photocatalytic degradation of fluoroquinolone, *Chem. Eng. J.* 442 (2022), <https://doi.org/10.1016/j.cej.2022.135943>.
- [36] X. Wu, C. Zhang, Z. Nie, Y. Zhang, Q. Bai, Z. Yin, S. Zhang, X. Qu, F. Du, L. Shi, Cookies-like Ag₂S/Bi₄NbO₈Cl heterostructures for high efficient and stable photocatalytic degradation of refractory antibiotics utilizing full-spectrum solar

- energy, Sep. Purif. Technol. 292 (2022), <https://doi.org/10.1016/j.seppur.2022.120969>.
- [37] H. Li, F. Deng, Y. Zheng, L. Hua, C. Qu, X. Luo, Visible-light-driven Z-scheme rGO/Bi₂S₃-BiOBr heterojunctions with tunable exposed BiOBr (102) facets for efficient synchronous photocatalytic degradation of 2-nitrophenol and Cr(vi) reduction, Environ. Sci. Nano 6 (12) (2019) 3670–3683, <https://doi.org/10.1039/c9en00957d>.
- [38] H.L. So, W. Chu, W. Xu, Photocatalysis of naphthalene by Fe₃O₄/Oxone/UV: simultaneous radical and non-radical pathways, J. Environ. Chem. Eng. 9 (2) (2021), <https://doi.org/10.1016/j.jece.2021.105076>.
- [39] H.M. El-Bery, H.N. Abdelhamid, Photocatalytic hydrogen generation via water splitting using ZIF-67 derived Co₃O₄@C/TiO₂, J. Environ. Chem. Eng. 9 (4) (2021), <https://doi.org/10.1016/j.jece.2021.105702>.
- [40] R.M. Mohamed, A.A. Ismail, A.S. Basaleh, H.A. Bawazir, Controllable synthesis of PtO modified mesoporous Co₃O₄ nanocrystals as a highly effective photocatalyst for degradation of Foron Blue dye, J. Photochem. Photobiol. A Chem. 428 (2022), <https://doi.org/10.1016/j.jphotochem.2022.113859>.
- [41] L. Li, C. Guo, J. Shen, J. Ning, Y. Zhong, Y. Hu, Construction of sugar-gourd-shaped CdS/Co_{1-x}S hollow hetero-nanostructure as an efficient Z-scheme photocatalyst for hydrogen generation, Chem. Eng. J. 400 (2020), <https://doi.org/10.1016/j.cej.2020.125925>.
- [42] R.R. Nallapureddy, M.R. Pallavolu, J. Nallapureddy, A.K. Yedluri, S.W. Joo, Z-scheme photocatalysis and photoelectrochemical platform with a Co₃O₄-CuO heterogeneous catalyst for the removal of water pollutants and generation of energy, J. Clean. Prod. 382 (2023), <https://doi.org/10.1016/j.jclepro.2022.135302>.
- [43] D. Sun, W. Fan, F. Wang, Y. Bai, H. Bai, W. Shi, Promoting photoelectrochemical hydrogen production performance by fabrication of Co_{1-x}S decorating BiVO₄ photoanode, Int. J. Hydrog. Energy 47 (2) (2022) 940–949, <https://doi.org/10.1016/j.ijhydene.2021.10.075>.
- [44] W. He, L. Liu, T. Ma, H. Han, J. Zhu, Y. Liu, Z. Fang, Z. Yang, K. Guo, Controllable morphology CoFe₂O₄/g-C₃N₄ p-n heterojunction photocatalysts with built-in electric field enhance photocatalytic performance, Appl. Catal. B Environ. 306 (2022), <https://doi.org/10.1016/j.apcatb.2022.121107>.
- [45] U. Sim, J. Moon, J. An, J.H. Kang, S.E. Jeong, J. Moon, S.-P. Cho, B.H. Hong, K. T. Nam, N-doped graphene quantum sheets on silicon nanowire photocathodes for hydrogen production, Energy Environ. Sci. 8 (4) (2015) 1329–1338, <https://doi.org/10.1039/c4ee03607g>.
- [46] L. Wang, B. Zhu, J. Zhang, J.B. Ghasemi, M. Mousavi, J. Yu, S-scheme heterojunction photocatalysts for CO₂ reduction, Matter 5 (12) (2022) 4187–4211, <https://doi.org/10.1016/j.matt.2022.09.009>.
- [47] X. Zhang, K. Yue, R. Rao, J. Chen, Q. Liu, Y. Yang, F. Bi, Y. Wang, J. Xu, N. Liu, Synthesis of acidic MIL-125 from plastic waste: significant contribution of N orbital for efficient photocatalytic degradation of chlorobenzene and toluene, Appl. Catal. B Environ. 310 (2022), <https://doi.org/10.1016/j.apcatb.2022.121300>.
- [48] J. Yu, X. Wang, L. Chen, G. Lu, G. Shi, X. Xie, Y. Wang, J. Sun, Enhanced adsorption and visible-light photocatalytic degradation of toluene by CQDs/UiO-66 MOG with hierarchical pores, Chem. Eng. J. 435 (2022), <https://doi.org/10.1016/j.cej.2022.135033>.
- [49] Z. Yuan, Y. Cao, Y. Meng, G. Pan, Y. Zheng, Z. Ni, S. Xia, The construction of lattice-matched CdS-Ag₂S heterojunction photocatalysts: high-intensity built-in electric field effectively boosts bulk-charge separation efficiency, J. Hazard. Mater. 458 (2023) 131895, <https://doi.org/10.1016/j.jhazmat.2023.131895>.
- [50] F. Guo, W. Shi, H. Wang, H. Huang, Y. Liu, Z. Kang, Fabrication of a CuBi₂O₄/g-C₃N₄ p-n heterojunction with enhanced visible light photocatalytic efficiency toward tetracycline degradation, Inorg. Chem. Front. 4 (10) (2017) 1714–1720, <https://doi.org/10.1039/c7qi00402h>.
- [51] H. Chen, S. Gao, G. Huang, Q. Chen, Y. Gao, J. Bi, Built-in electric field mediated S-scheme charge migration in COF/In₂S₃ heterojunction for boosting H₂O₂ photosynthesis and sterilization, Appl. Catal. B: Environ. 343 (2024), <https://doi.org/10.1016/j.apcatb.2023.123545>.
- [52] H. Han, W. Wang, L. Yao, C. Hao, Y. Liang, J. Fu, P. Zeng, Photostable 3D heterojunction photoanode made of ZnO nanosheets coated onto TiO₂ nanowire arrays for photoelectrochemical solar hydrogen generation, Catal. Sci. Technol. 9 (8) (2019) 1989–1997, <https://doi.org/10.1039/c9cy00119k>.
- [53] L. Wang, Y. Hu, F. Qi, L. Ding, J. Wang, X. Zhang, Q. Liu, L. Liu, H. Sun, P. Qu, Anchoring black phosphorus nanoparticles onto ZnS porous nanosheets: efficient photocatalyst design and charge carrier dynamics, ACS Appl. Mater. Interfaces 12 (7) (2020) 8157–8167, <https://doi.org/10.1021/acsaami.9b19408>.
- [54] Z. Miao, Q. Wang, Y. Zhang, L. Meng, X. Wang, In situ construction of S-scheme AgBr/BiOBr heterojunction with surface oxygen vacancy for boosting photocatalytic CO₂ reduction with H₂O, Appl. Catal. B Environ. 301 (2022), <https://doi.org/10.1016/j.apcatb.2021.120802>.
- [55] J.T. Schneider, D.S. Firak, R.R. Ribeiro, P. Peralta-Zamora, Use of scavenger agents in heterogeneous photocatalysis: truths, half-truths, and misinterpretations, Phys. Chem. Chem. Phys. 22 (27) (2020) 15723–15733, <https://doi.org/10.1039/d0cp02411b>.
- [56] Z. Zhang, J. Huang, Y. Fang, M. Zhang, K. Liu, B. Dong, A nonmetal plasmonic Z-scheme photocatalyst with UV- to NIR-driven photocatalytic protons reduction, Adv. Mater. 29 (18) (2017), <https://doi.org/10.1002/adma.201606688>.
- [57] R. Xie, K. Fang, Y. Liu, W. Chen, J. Fan, X. Wang, Y. Ren, Y. Song, Z-scheme In₂O₃/WO₃ heterogeneous photocatalysts with enhanced visible-light-driven photocatalytic activity toward degradation of organic dyes, J. Mater. Sci. 55 (26) (2020) 11919–11937, <https://doi.org/10.1007/s10853-020-04863-5>.
- [58] Z. Pan, L. Qian, J. Shen, J. Huang, Y. Guo, Z. Zhang, Construction and application of Z-scheme heterojunction In₂O₃/Bi₄O₇ with effective removal of antibiotic under visible light, Chem. Eng. J. 426 (2021), <https://doi.org/10.1016/j.cej.2021.130385>.
- [59] Y. Wang, X. Li, S. Liu, Y. Liu, T. Kong, H. Zhang, X. Duan, C. Chen, S. Wang, Roles of catalyst structure and gas surface reaction in the generation of hydroxyl radicals for photocatalytic oxidation, ACS Catal. 12 (5) (2022) 2770–2780, <https://doi.org/10.1021/acscatal.1c05447>.
- [60] X. Ruan, C. Huang, H. Cheng, Z. Zhang, Y. Cui, Z. Li, T. Xie, K. Ba, H. Zhang, L. Zhang, Y. Zhao, J. Leng, S. Jin, W. Zhang, W. Zheng, S.K. Ravi, Z. Jiang, X. Cui, J. Yu, A twin S-scheme artificial photosynthetic system with self-assembled heterojunctions yields superior photocatalytic hydrogen evolution rate, Adv. Mater. 35 (6) (2023) e2209141, <https://doi.org/10.1002/adma.202209141>.
- [61] S. Wang, Z. Li, G. Yang, Y. Xu, Y. Zheng, S. Zhong, Y. Zhao, S. Bai, Embedding nano-piezoelectrics into heterointerfaces of S-scheme heterojunctions for boosting photocatalysis and piezophotocatalysis, Small 19 (42) (2023) e2302717, <https://doi.org/10.1002/smll.202302717>.
- [62] C. Deng, F. Ye, T. Wang, X. Ling, L. Peng, H. Yu, K. Ding, H. Hu, Q. Dong, H. Le, Y. Han, Developing hierarchical CdS/NiO hollow heterogeneous architectures for boosting photocatalytic hydrogen generation, Nano Res. 15 (3) (2021) 2003–2012, <https://doi.org/10.1007/s12274-021-3960-4>.
- [63] Y. Wang, C. Yang, K. Zhang, L. Guo, R. Li, A. Zaheer, F. Fu, B. Xu, D. Wang, In-situ construction of 2D/2D CuCo₂S₄/Bi₂WO₆ contact heterojunction as a visible-light-driven fenton-like catalyst with highly efficient charge transfer for highly efficient degradation of tetracycline hydrochloride, Colloids Surf. A Physicochem. Eng. Asp. 634 (2022), <https://doi.org/10.1016/j.colsurfa.2021.127965>.
- [64] Z. Zhang, J. Liang, W. Zhang, M. Zhou, X. Zhu, Z. Liu, Y. Li, Z. Guan, C.-S. Lee, P. K. Wong, H. Li, Z. Jiang, Modified-pollen confined hybrid system: a promising union for visible-light-driven photocatalytic antibiotic degradation, Appl. Catal. B Environ. 330 (2023), <https://doi.org/10.1016/j.apcatb.2023.122621>.
- [65] Y. Liu, G. Li, D. Wang, Z. Zhong, K. Hu, C. Zhang, G. Hu, X. Li, Y. Wan, Lanthanide-doped upconversion glass-ceramic photocatalyst fabricated from fluorine-containing waste for the degradation of organic pollutants, J. Colloid Interface Sci. 638 (2023) 461–474, <https://doi.org/10.1016/j.jcis.2023.01.142>.
- [66] Z. Huang, H. Liu, Insights into the pathways, intermediates, influence factors and toxicological properties in the degradation of tetracycline by TiO₂-based photocatalysts, J. Environ. Chem. Eng. 11 (5) (2023), <https://doi.org/10.1016/j.jece.2023.110587>.
- [67] F. Zhang, J. Xin, X. Wu, J. Liu, L. Niu, D. Wang, X. Li, C. Shao, X. Li, Y. Liu, Floating metal phthalocyanine@polyacrylonitrile nanofibers for peroxymonosulfate activation: synergistic photothermal effects and highly efficient flowing wastewater treatment, J. Hazard. Mater. 459 (2023) 132228, <https://doi.org/10.1016/j.jhazmat.2023.132228>.